

The Evolving Magnetic Topology of τ Boötis

M. W. Mengel,^{1*} R. Fares,² S. C. Marsden,¹ B. D. Carter,¹ S. V. Jeffers,³
P. Petit,^{4,5} J.-F. Donati,^{4,5} C. P. Folsom^{6,7} and the BCoolest Collaboration

¹Computational Engineering & Science Research Centre, University of Southern Queensland, Toowoomba, Qld, Australia

²School of Physics and Astronomy, University of St Andrews, St Andrews KY16 9SS, UK

³Institut für Astrophysik, Georg-August-Universität Göttingen, Friedrich-Hund-Platz 1, 37077 Göttingen, Germany

⁴Université de Toulouse, UPS-OMP, Institut de Recherche en Astrophysique et Planétologie, F-31400 Toulouse, France

⁵CNRS, Institut de Recherche en Astrophysique et Planétologie, 14 Avenue Edouard Belin, F-31400 Toulouse, France

⁶Université Grenoble Alpes, IPAG, F-38000 Grenoble, France

⁷CNRS, IPAG, F-38000 Grenoble, France

Accepted 2016 April 7. Received 2016 April 5; in original form 2015 November 9

ABSTRACT

We present six epochs of spectropolarimetric observations of the hot-Jupiter-hosting star τ Boötis that extend the exceptional previous multi-year data set of its large-scale magnetic field. Our results confirm that the large-scale magnetic field of τ Boötis varies cyclicly, with the observation of two further magnetic reversals; between December 2013 and May 2014 and between January and March 2015. We also show that the field evolves in a broadly solar-type manner in contrast to other F-type stars. We further present new results which indicate that the chromospheric activity cycle and the magnetic activity cycles are related, which would indicate a very rapid magnetic cycle. As an exemplar of long-term magnetic field evolution, τ Boötis and this long-term monitoring campaign presents a unique opportunity for studying stellar magnetic cycles.

Key words: stars: activity - stars: imaging - stars: individual: τ Boo - stars: magnetic fields - techniques: polarimetric - planetary systems.

1 INTRODUCTION

Magnetic fields of planet-hosting stars are of significant interest given the expected role of the magnetic field in both stellar and planetary system evolution. τ Boötis (HR 5185, HD 120136, F7V, age ~ 1 Gyr; list of stellar parameters given in Table 1) hosts a hot Jupiter with a mass of $\sim 6M_{Jupiter}$ (Rodler et al. 2012; Brogi et al. 2012; Borsa et al. 2015) orbiting at 0.049 AU in approximately 3.31 days (Butler et al. 1997; Leigh et al. 2003; Borsa et al. 2015) and has been the subject of periodic observation of its magnetic field since 2007. This unique long-term spectropolarimetric observational series of τ Boötis has allowed the investigation of the evolution of its magnetic topology over an extended period.

Donati et al. (2008) and Fares et al. (2009, 2013) have observed that τ Boötis exhibits a magnetic cycle including polarity reversals occurring roughly on a yearly timescale. Studies of younger stars which like τ Boötis have shallow convective zones (Jeffers et al. 2011; Jeffers & Donati 2008; Marsden et al. 2006), have not shown magnetic cycles; per-

haps because the duration of the cycles are longer than the periods of observation or because their cycles are irregular or chaotic. Fares et al. (2009) speculate that the hot Jupiter with $M_p \sim 6M_{Jupiter}$ (compared to the stellar convective envelope with a mass of $\sim 0.5M_{Jupiter}$) may accelerate the stellar magnetic activity cycle by synchronising the outer convective envelope of the star (due to tidal interactions) and enhancing the shear at the tachocline.

τ Boötis has been a target of interest for those searching for star-planet interaction (SPI). Photometric observations from the *MOST* satellite by Walker et al. (2008) suggested that a persistent active region exists on the star synchronised with the period of the hot Jupiter, but leading the subplanetary longitude by $\sim 68^\circ$. The presence of a persistent active region may suggest star-planet interaction (SPI). Lanza (2012) contends that models rule out that any such “hot spots” are due to magnetic SPI, and therefore if truly related to the planetary period they must be via some other mechanism. Given that the orbital period of the planet τ Boötis b and the star’s rotational period are presumed to be synchronized, observations of the star may not resolve whether or not any rotationally modulated chromospheric features are indicative of SPI or not.

* E-mail: matthew.mengel@usq.edu.au (MWM)

Table 1. Table of stellar parameters for τ Boötis. (References: 1 = [Borsa et al. \(2015\)](#); 2 = [Brogi et al. \(2012\)](#))

Parameter		Value	Reference
T_{eff}	(K)	6399 ± 45	1
$\log g$	(cm s^{-1})	4.27 ± 0.06	1
[Fe/H]		0.26 ± 0.03	1
$v \sin i$	(km s^{-1})	14.27 ± 0.06	1
Luminosity	(L_{\odot})	3.06 ± 0.16	1
Mass	(M_{\odot})	1.39 ± 0.25	1
Radius	(R_{\odot})	1.42 ± 0.08	1
Age	(Gyr)	0.9 ± 0.5	1
Inclination	($^{\circ}$)	44.5 ± 1.5	2

More recently, [Borsa et al. \(2015\)](#) analysed spectra of τ Boötis using the HARPS-N spectrograph. Their study suggests that a high-latitude plage was present near one pole of the star. While [Borsa et al. \(2015\)](#) conclude that “it is unclear if it is due to SPI or to a corotating active region, or both”, this observation is particularly interesting as it overlaps with one of the epochs presented in this work and is discussed in the conclusion.

We present in this paper a new set of epochs to extend the spectropolarimetric study of τ Boötis as part of the BCool collaboration¹ on the magnetic fields of cool stars. Radial magnetic maps from previous epochs of observation have been used as boundary conditions for modelling the wind environment around the star ([Vidotto et al. 2012](#)). Similarly, work presented here provides these boundary conditions for an ongoing monitoring of the stellar wind of τ Boötis ([Nicholson et al. 2016](#)).

Investigation of the Ca II H&K stellar activity proxy of the star is shown in Section 3. Modelling of the large-scale magnetic field of the star, including its differential rotation is presented in Section 4. We draw conclusions in Section 5.

2 OBSERVATIONS AND DATA PROCESSING

Stokes V spectropolarimetric data of τ Boötis were obtained in May 2011 using the HARPS polarimeter (hereafter referred to as HARPSpol) and in 2013, 2014 and 2015 using the NARVAL high-resolution spectropolarimeter. Each Stokes V spectrum is derived from a sequence of four sub-exposures taken with the waveplates (HARPSpol)/retarder rhombs (NARVAL) of the polarimeters in different positions ([Semel et al. 1993](#); [Donati et al. 1997](#)). The phases of the data are derived using the same orbital ephemeris as that used by [Catala et al. \(2007\)](#), [Donati et al. \(2008\)](#), [Fares et al. \(2009\)](#) and [Fares et al. \(2013\)](#):

$$T_0 = \text{HJD } 2453450.984 + 3.31245E \quad (1)$$

with phase 0.0 denoting the first conjunction (i.e. the planet furthest from the observer).

¹ <http://bcool.ast.obs-mip.fr>

³ <http://www.eso.org/sci/facilities/lasilla/instruments/harps/inst/performance.html>

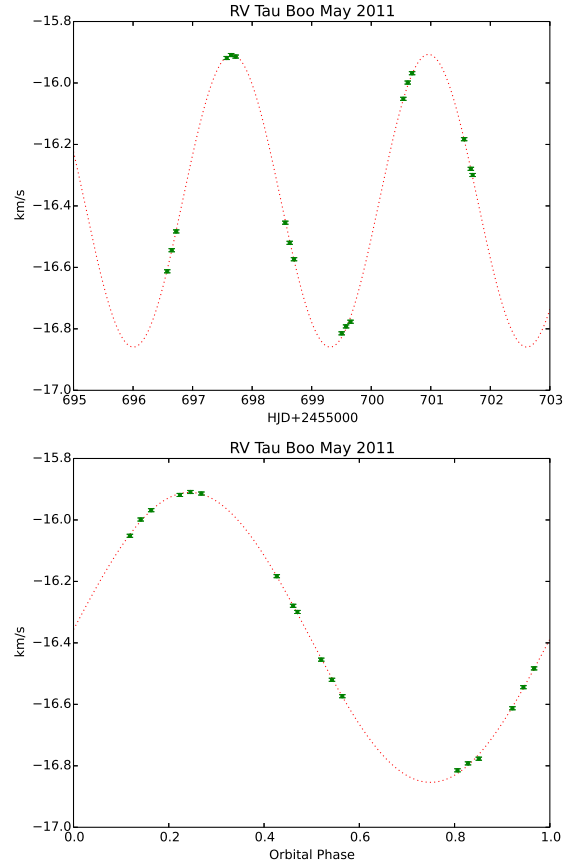


Figure 1. Radial velocity of τ Boötis, May 2011 derived from HARPSpol data as a function of HJD (upper panel) and as a function of orbital phase (lower panel). The errors in the measurements are $\sim 5 \text{ m s}^{-1}$, which is the approximate error for HARPSpol in pure spectroscopic mode ([Mayor et al. \(2003\)](#)) and the accompanying HARPS performance summary³. The fitted semi-amplitude of 476 m s^{-1} is close to that in [Butler et al. \(1997\)](#).

2.1 Observations with HARPSpol

HARPSpol ([Piskunov et al. 2011](#)) is located at the ESO 3.6-m telescope at La Silla. HARPSpol has a spectral resolution of around 110000, with spectral coverage from 380 nm to 690 nm. In May 2011, 18 spectra were collected over six nights using HARPSpol, providing good coverage of the complete rotational cycle. The journal of observations from May 2011 is shown in Table B1.

2.2 Observations with NARVAL

NARVAL is attached to the 2-m T el escope Bernard Lyot (TBL) at Pic du Midi. A twin of the CFHT ESPaDOnS instrument ([Donati 2003](#)), NARVAL has a spectral coverage of 370 nm to 1048 nm with a resolution of approximately 65000. Information on NARVAL can be found in [Auri ere \(2003\)](#).

From April 23 until May 13 2013 (approximately 21 nights) eight observations were taken using NARVAL. The coverage of the stellar cycle was incomplete, with two observations close to $\phi_{\text{rot}} \sim 0.25$ and the remaining six giving relatively even coverage of $0.5 < \phi_{\text{rot}} < 1$. Twelve observations were taken using NARVAL from December 4 until

December 21 2013 (17 nights). The coverage of the stellar surface was sparse but relatively complete. Eleven observations were taken using NARVAL between May 4 and May 18 2014 (14 nights). In January 2015, seven observations were obtained using NARVAL over 12 nights. The journal of observations from April 2013 through January 2015 is shown in Table B2.

Beginning in March 2015 a further series of observations of τ Boötis were obtained. The observations were more sparsely separated and spanned a significant period of time (~ 70 d, ~ 22 rotations). Given that this period is considered too long for a single ZDI analysis due to potential for feature evolution, this data set was divided into multiple overlapping epochs and analysed separately. Thus this observational data is presented in its own journal of observations (Table B3).

2.3 Data Reduction

Data from NARVAL was automatically reduced using the LIBRE-ESPRIT software package. A specifically modified version of LIBRE-ESPRIT was used by JFD to reduce the data from HARPSpol. LIBRE-ESPRIT produces Stokes I (unpolarized) and Stokes V (circularly polarized) spectra, in addition to a null (N) spectrum which is used to determine the authenticity of a detected polarization signal (Donati et al. 1997).

2.3.1 Least Squares Deconvolution (LSD)

As Zeeman signatures are typically smaller than the noise level within a single spectral line, they are difficult to detect, especially for solar-type stars such as τ Boötis. The Least Squares Deconvolution (LSD) technique is applied to improve the S/N of the data by combining the information provided by many spectral lines (Donati et al. 1997). The line mask used to perform the deconvolution is the same as described in Donati et al. (2008) and Fares et al. (2009), using a Kurucz model atmosphere with solar abundances, an effective temperature of 6250 K and $\log g$ of 4.0 cm s^{-2} , including most strong lines in the optical domain (central depths $> \sim 40$ percent of the local continuum before macroturbulent or rotational broadening) but excluding the strongest, broadest features such as Balmer lines. This results in each deconvolution utilizing 3000-4000 lines, depending on the particular spectral coverage of the instrument.

In the journals of observations (Tables B1, B2, B3), a definite detection (D) in the LSD Stokes V profile is defined as a false alarm probability (*fap*) of less than 10^{-5} . A marginal detection (M) has a false alarm probability greater than 10^{-5} but less than 10^{-3} (Donati et al. 1997).

2.3.2 Radial Velocity

Due to the presence of the hot Jupiter in orbit around τ Boötis, the radial velocity (RV) of the star varies from observation to observation. The best-fit semi-amplitude of 476 m s^{-1} we derive is close to that found by Butler et al. (1997) and in good agreement with the expected phasing using the orbital ephemeris of Catala et al. (2007) (See Fig. 1 for May 2011 observations). The spectra are automatically

Table 2. Table of coefficients for Equation 2 as calculated by Marsden et al. (2014) for the NARVAL instrument.

Coefficient	NARVAL
<i>a</i>	12.873
<i>b</i>	2.502
<i>c</i>	8.877
<i>d</i>	4.271
<i>e</i>	1.183×10^{-3}

corrected by the LIBRE-ESPRIT software for RV variations due to the motion of the Earth. The RV of the star due to the orbital motion of the system is derived by fitting the Stokes I LSD profile of each observation with a Gaussian and determining the centre of the profile. The spectra are then corrected for the RV due to the system's orbital motion.

3 CA II H & K ACTIVITY PROXY

The emission in the cores of the Ca II H & K lines is one of the most widely used proxies for stellar chromospheric activity. The S-index for each observation of τ Boötis was calculated using the method of Wright et al. (2004) and utilizing the coefficients for NARVAL derived by Marsden et al. (2014) for the equation:

$$\text{S-index} = \text{Ca}_{\text{HK}}\text{-index} = \frac{aF_H + bF_K}{cF_{R_{\text{HK}}} + dF_{V_{\text{HK}}}} + e \quad (2)$$

where F_H and F_K are the fluxes in a 2.18\AA triangular bandpasses centred on the cores of the Ca II H & K lines, $F_{R_{\text{HK}}}$ and $F_{V_{\text{HK}}}$ are rectangular 20\AA bandpasses centred on the continuum at 3901.07\AA and 4001.07\AA (Wright et al. 2004, Fig. 1). These coefficients for the NARVAL instrument are shown in Table 2.

Following the methodology of Marsden et al. (2014), overlapping orders were removed from the reduced spectra of τ Boötis and adjusted for the radial velocity for the observation. In addition to the newly observed epochs, all prior observations of τ Boötis with the NARVAL instrument were retrieved from the Polarbase⁴ (Petit et al. 2014) database, and we calculated values of the S-index for each normalised individual exposure of τ Boötis, making four data points for each spectropolarimetric sequence. These are shown in Figure 2. As noted in Fares et al. (2009), τ Boötis exhibits intrinsic variability through each night and night-to-night, and this can be observed in the data. Using a least-squares fit of a sinusoid to the unweighted S-index data we find a longer-term variability in chromospheric activity of ~ 117 d. This result corresponds well to the ~ 116 d period reported by Baliunas et al. (1997) and Henry et al. (2000) from the Mount Wilson HK project (Baliunas et al. 1998).

There also appears to be a longer-term trend apparent in the data. Baliunas et al. (1997) reports a low-amplitude 11.6 yr activity cycle, however our data set is too short to reliably perform a fit of that duration. In attempting to fit multiple periods, various results converged depending upon initial conditions. There are several fits of equally good quality with different periodicities from approximately ~ 300 d

⁴ <http://polarbase.irap.omp.eu/>

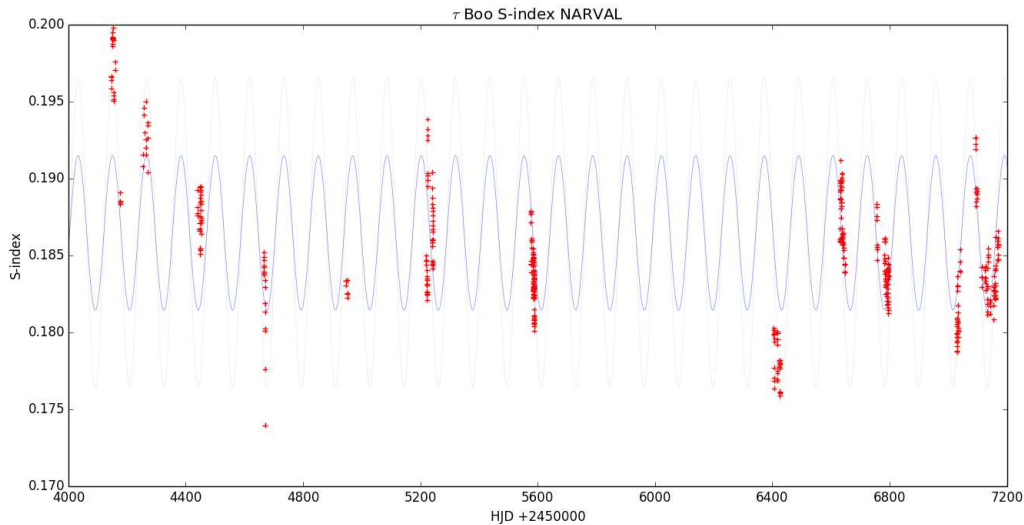


Figure 2. Ca II HK S-indices for τ Boötis. NARVAL observations are shown in red. A least-squares fit of a sinusoid to the unweighted data (blue line) yields a period of ~ 117 d, which corresponds closely to the ~ 116 d period reported by Baliunas et al. (1997); Henry et al. (2000).

to several thousand days and given the large gaps in the observational records, these periods are uncertain. Further observational epochs taken at shorter intervals are required to accurately characterise the cyclic behaviour of the Ca II H & K activity proxy of τ Boötis and if any relationship to other observed cycles exists.

4 MAGNETIC MAPPING

4.1 Model Description

Zeeman Doppler Imaging (ZDI) is used to reconstruct maps of the magnetic topology of τ Boötis from the observed Stokes V signatures (Fig. 6). The process uses the principles of maximum entropy image reconstruction to produce the configuration of the large-scale magnetic field containing the minimum information required to produce the observed magnetic signatures. The code used is that described in Donati et al. (2006) wherein spherical-harmonic expansions are used to describe the field configuration with respect to its poloidal and toroidal components. An advantage of this method is that the coefficients of the spherical harmonics can be used to calculate the energy contained in, for example, axisymmetric and non-axisymmetric modes, and to determine relative contributions of dipolar, quadrupolar and higher-order components.

The stellar surface is divided into units of similar projected area and the contribution of each unit area to the Stokes V profile (based on field strength, orientation, surface location and motion) is calculated. The process continues iteratively wherein profiles are reconstructed and compared to the observed profiles until a match within the desired error is reached (typically a unit reduced χ^2 ; i.e. $\chi_r^2 \sim 1$).

The local Stokes I profile is modelled by a Gaussian (FWHM of 11 km s^{-1}), while the local Stokes V is calculated assuming the weak field approximation (Donati et al. 1997):

$$V \propto g B_{los} \frac{dI}{dv} \quad (3)$$

where B_{los} is the local line-of-sight component of the magnetic field and g is the mean Landé factor.

4.2 Differential Rotation

4.2.1 Method

When a star is differentially rotating, the signatures produced by magnetic regions will repeat from rotational cycle to rotational cycle but with differences resulting from shifts in the relative location of the regions due to the differential rotation. We consider that the rotation will follow a simplified solar-type law:

$$\Omega(\theta) = \Omega_{eq} - d\Omega \sin^2 \theta \quad (4)$$

where $\Omega(\theta)$ is the rotation rate of the star at latitude θ in rad d^{-1} , Ω_{eq} is the rotation rate at the equator and $d\Omega$ is the rotational shear between the equator and the poles.

Applying the method described by Donati et al. (2000), Petit et al. (2002), Donati et al. (2003) and Morin et al. (2008) we construct a magnetic image containing a given information content for each pair of $(\Omega_{eq}, d\Omega)$ and choose the pair of parameters which produces the best fit to the data (i.e. the smallest χ_r^2). An example for the December 2013 data set is shown in Figure 3(a). Figure 3(b) shows how we derive $\sim 1\text{-}\sigma$ variation bars as a measure of uncertainty by varying various stellar parameters ($v \sin i \pm 1 \text{ km s}^{-1}$; inclination $\pm 10^\circ$; target reconstructed average magnetic field $B_{mod} \pm \sim 10\%$) and calculating the extreme variations.

Donati et al. (2008) measured the differential rotation of τ Boötis utilizing the Stokes V data, equal to $\Omega_{eq} = (2.10 \pm 0.04) \text{ rad d}^{-1}$ and $d\Omega = (0.50 \pm 0.12) \text{ rad d}^{-1}$. How-

ever, subsequent observations have yielded either different values of Ω_{eq} and $d\Omega$ (e.g. January 2008, $d\Omega = 0.28 \pm 0.10$; Fares et al. (2009)) or no measurement has been possible (Fares et al. 2013).

4.2.2 Results

The May 2011 HARPSpol data produced a well-defined paraboloid, albeit with a larger error compared to other runs. The HARPSpol data is of a lower S/N than that from NARVAL, however the May 2011 phase coverage is superior to the other runs. The derived parameters of $\Omega_{eq} = 2.03^{+0.05}_{-0.05}$ and $d\Omega = 0.42^{+0.11}_{-0.11}$ rad d⁻¹ is consistent with those of Donati et al. (2008).

For the NARVAL data from April/May 2013, we measure a significant error bar. The maps for April-May 2013 show that there are only two observations of the star consistent with phase ~ 0.25 (ϕ_{rot} of -2.749 and +3.262), and these are separated by ~ 6 full rotations (~ 20 d). Removing these observations results in a smaller error and a lower value of $d\Omega$. However, the DR measurement used in our mapping and reported in Table 3 is made with all observations present, hence a much larger error is calculated. The derived parameters for April/May 2013 were $\Omega_{eq} = 2.05^{+0.04}_{-0.04}$ and $d\Omega = 0.38^{+0.18}_{-0.19}$ rad d⁻¹.

With a better coverage of the stellar rotational cycle in December 2013, a clear paraboloid was again generated (Fig. 3(a)). The measured differential rotation for December 2013 corresponded to parameters of $\Omega_{eq} = 1.95^{+0.01}_{-0.01}$ rad d⁻¹ and $d\Omega = 0.16^{+0.04}_{-0.04}$ rad d⁻¹.

The data for May 2014 once more produced a clear paraboloid with the parameters $\Omega_{eq} = 1.99^{+0.01}_{-0.01}$ rad d⁻¹ and $d\Omega = 0.10^{+0.04}_{-0.04}$ rad d⁻¹. Finally, the derived parameters for January 2015 were $\Omega_{eq} = 1.98^{+0.03}_{-0.03}$ rad d⁻¹ and $d\Omega = 0.15^{+0.15}_{-0.16}$ rad d⁻¹.

These values are summarised in Table 3.

4.2.3 A discussion of variable Differential Rotation measurement

Table 3 makes clear that the technique used to determine differential rotation yields a wide variation in $d\Omega$, but is consistent with solar-like differential rotation with the equator rotating faster than the poles. Ω_{eq} is much more constrained within a range from ~ 1.95 rad d⁻¹ to 2.05 rad d⁻¹, ignoring the error. As simulations performed by Petit et al. (2002) show, factors including the phase coverage and observational cadence can have significant effects on the measured differential rotation parameters.

Notably, apart from the May 2011 HARPSpol observation, at best the observations of τ Boötis have had a single observation per night (approximately one 4×600 s observation every one-third of a rotation) over several full stellar rotations. As the technique used to determine differential rotation is a χ^2 -landscape technique and dependent upon the regular re-observation of features, it is possible that the significant variation in the measured parameters are due to observational biases. The weakness of the field of τ Boötis and the difficulty in observing Zeeman signatures on the star potentially exacerbates this effect. Attempting the χ^2 minimisation method with lower values of target B_{mod} with

various τ Boötis data sets, (corresponding to higher χ_r^2 fits) thus providing less information for the technique produces a systemic decrease in the calculated values of Ω_{eq} and $d\Omega$.

This supposition would need to be confirmed by simulations and it should be noted that this does not rule out the existence of small or significant actual variation in differential rotation of magnetic features on τ Boötis; simply that we cannot draw any such conclusion from these measurements. A paper is in preparation (Mengel et. al.) examining the effect of phase coverage on measuring DR parameters on slow rotating weak-field stars and how we may determine optimal observational cadences and periods for this type of target.

Finally, it is to be noted that varying $d\Omega$ will slightly distort the shape of the features on the maps but does not appear to have a significant effect in the determination of the general magnetic field properties (Table 6). Consequently to be internally consistent in applying the maximum-entropy, minimum information mapping technique, these measured values for $d\Omega$ and Ω_{eq} which give the minimum information solution have been utilised in the magnetic mapping in this work.

4.2.4 Stokes I Differential Rotation - Fourier Transform Method

An alternative measurement of the differential rotation can be made using the Fourier Transform (FT) method described by Reiners & Schmitt (2003).

An averaged Stokes I profile was created from the NARVAL and HARPSpol data for each observational epoch. Using the method of Reiners & Schmitt (2003), we obtained the ratio of the first two zeros of the Fourier transformed average Stokes I line profile (q_2/q_1). An example of this is shown for the May 2014 epoch in Fig. 4. For each epoch, we determined that $q_2/q_1 = 1.61 \pm 0.07$. From Equation 5 in Reiners & Schmitt (2003), using an inclination angle of 45° we thus calculate α ($d\Omega/\Omega_{eq}$) of ≈ 0.17 .

Using the various measured values of Ω_{eq} from Table 3, this produces a value for $d\Omega$ of between 0.34 rad d⁻¹ and 0.36 rad d⁻¹, which is in good agreement with the value found by Reiners (2006), Catala et al. (2007), and Borsa et al. (2015) for τ Boötis.

It is noted that this technique is quite sensitive to the derived value of q_2/q_1 . Thus using $q_2/q_1 = 1.61 \pm 0.07$ would yield an uncertainty in $d\Omega$ of 0.14 rad d⁻¹. Again, this uncertainty is in agreement with the measurements of the differential rotation of τ Boötis by Reiners (2006).

Yielding a value of $d\Omega = 0.35 \pm 0.14$ rad d⁻¹, the Fourier transform method is broadly consistent with the values derived by the χ^2 -landscape method taking into account the errors calculated for both methods. Despite the consistency of the two methods described here, the differential rotation measurement must be viewed with caution due to the uncertainties and assumptions inherent in each method.

4.3 Magnetic Mapping

4.3.1 Stellar and Model Parameters

Utilising the measured differential rotation parameters, a χ^2 minimization process was used to determine the optimum angle of inclination and $v \sin i$. The values derived were close

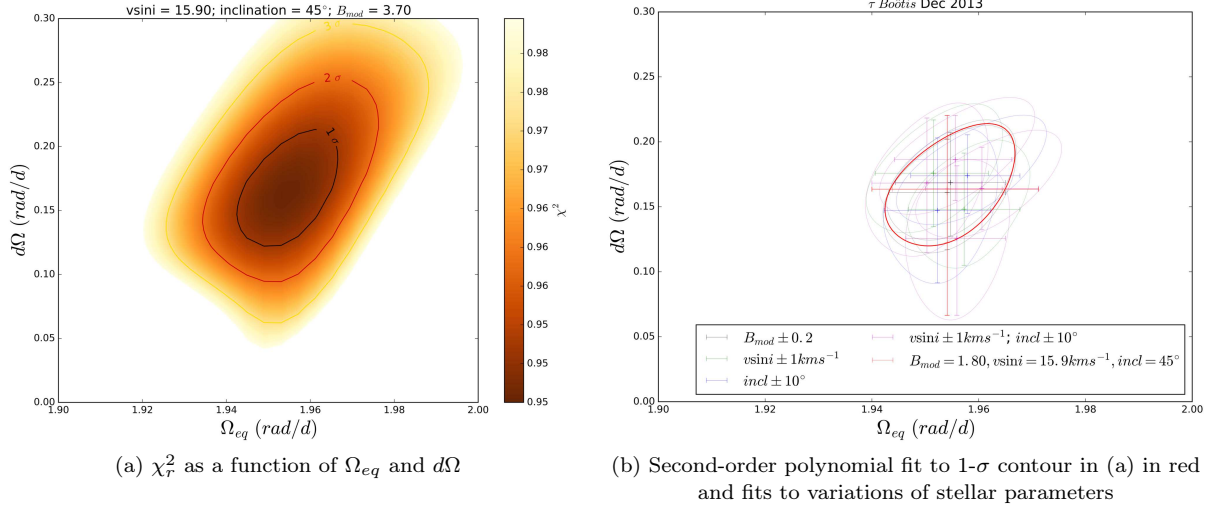


Figure 3. Differential rotation of τ Boötis for December 2013. Panel (a) shows the variation of χ_r^2 as a function of Ω_{eq} and $d\Omega$ for the selected stellar parameters ($v \sin i = 15.9 \text{ km s}^{-1}$, inclination 45°) and a target B_{mod} appropriate for the desired χ_r^2 used to reconstruct the magnetic maps of this epoch. Panel (b) shows second-order polynomial fits for the 1- σ threshold paraboloids surrounding the minimum χ_r^2 where the red paraboloid corresponds to the plot in panel (a). Other paraboloids represent fits to the corresponding DR calculations varying the target $B_{mod} (\pm \sim 10\%)$, $v \sin i (\pm 1 \text{ km s}^{-1})$ and stellar inclination ($\pm 10^\circ$) independently (green and blue) and $v \sin i$ and inclination angle together (magenta). The overall variation bars are used to derive the uncertainty in the measured DR parameters.

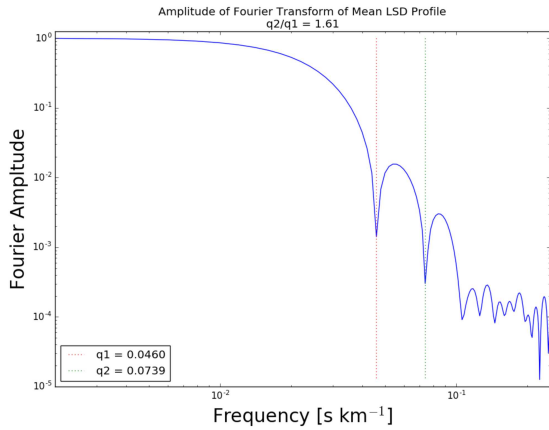


Figure 4. Amplitude of the Fourier transform of the averaged LSD Stokes I profile for May 2014. The first two zeros (q_1, q_2) are shown. The ratio q_2/q_1 can be used to derive α ($d\Omega/\Omega_{eq}$) as described in the text (Section 4.2.4).

to those used in previously published works (Fares et al. 2009, 2013) so an inclination of 45° and $v \sin i$ of 15.9 km s^{-1} as used in Fares et al. (2013) were chosen and applied to all data sets. (It is noted that this value of $v \sin i$ varies by $\sim 10\%$ from the latest published value shown in Table 1, however the difference in the models was insignificant using either value, thus we use the derived value for consistency with previous works).

Once the stellar parameters and differential rotation values were chosen, maps were generated for different values of χ_r^2 .

The reconstructed average magnetic field (B_{mod}) begins to rise significantly with a lower target χ_r^2 as the process begins fitting inappropriately to the noise inherent in

Table 3. Summary of differential rotation parameters for τ Boötis as measured by the χ^2 minimisation method. For comparison, the FT method (Sec. 4.2.4, assuming $\Omega_{eq} = 2.00 \text{ rad d}^{-1}$) yields $d\Omega = 0.35 \pm 0.14 \text{ rad d}^{-1}$. The values presented below are used in the magnetic mapping.

Epoch	Ω_{eq} rad d $^{-1}$	$d\Omega$ rad d $^{-1}$
2011 May	$2.03^{+0.05}_{-0.05}$	$0.42^{+0.11}_{-0.11}$
2013 April/May	$2.05^{+0.04}_{-0.04}$	$0.38^{+0.18}_{-0.19}$
2013 December	$1.95^{+0.01}_{-0.01}$	$0.16^{+0.04}_{-0.04}$
2014 May	$1.99^{+0.01}_{-0.01}$	$0.10^{+0.04}_{-0.04}$
2015 January	$1.98^{+0.03}_{-0.03}$	$0.15^{+0.15}_{-0.16}$

the signatures, this requires the target χ_r^2 to be chosen with care. This effect is much more pronounced in the HARPSpol data than for the NARVAL data and it would thus be inappropriate to utilise the same χ_r^2 for the May 2011 data. Thus a χ_r^2 was chosen to be 0.95 for the NARVAL data, and 1.10 for the HARPSpol data. A potential drawback of this is that the comparison of the absolute magnitude of the field strength may no longer be appropriate for the data sets derived from the different instruments or between data sets using the same instrument with significantly different S/N levels and thus target χ_r^2 .

The spherical harmonic expansions for the magnetic field were calculated using $\ell = 8$ as little improvement was obtained using $\ell > 8$, there being near to zero energy in higher order harmonics. This is consistent with previous papers dealing with τ Boötis and adequate given there are ~ 9 spatial resolution elements around the equator as per equation 5 (Morin et al. 2010, Eq. 3).

$$\frac{2\pi v_e \sin i}{\text{FWHM}} = \frac{2\pi(15.9 \text{ km s}^{-1})}{11 \text{ km s}^{-1}} \sim 9 \quad (5)$$

The amount of energy in the various harmonics can be used to describe the configuration of the magnetic field (Donati et al. 2006). These results, shown in Table 6 consist of three calculations. First, the amount of the magnetic energy stored in the toroidal component of the field is found from the $\gamma_{\ell,m}$ term of the complex coefficients of the spherical harmonics. Second, the amount of magnetic energy in the poloidal component ($\alpha_{\ell,m}$ and $\beta_{\ell,m}$) which is axisymmetric (i.e. symmetric about the axis of rotation) is found from the $\alpha_{\ell,m}$ and $\beta_{\ell,m}$ coefficients of the spherical harmonics where $m = 0$. (Other papers, such as Fares et al. (2009, 2013) use $m < \ell/2$ rather than $m = 0$. We consider $m = 0$ to be more mathematically correct, however the difference in practice is quite small so direct comparisons between epochs are possible. Where appropriate this is noted in the text). Finally, the amount of magnetic energy in the poloidal component of the magnetic field consisting of dipolar plus quadrupolar components is calculated from $\alpha_{\ell,m}$ and $\beta_{\ell,m}$ coefficients where $\ell \leq 2$.

As in the differential rotation measurements, an indication of the variation in these values is found by varying the differential rotation measurement by the error found for each epoch (holding inclination and $v \sin i$ constant), then varying the stellar parameters (inclination $\pm 10^\circ$; $v \sin i \pm 1.0 \text{ km s}^{-1}$) while holding $d\Omega$ and Ω_{eq} constant. It is noted that the variation of stellar parameters produces variation in field components in a consistent way across the epochs, and the variations, although sometimes large relative to the values are of the same order of magnitude across the epochs. The amount of toroidal field has the smallest variation due to parameter variation. The amount of energy in axisymmetric and $\ell \leq 2$ modes in the poloidal field exhibit large variability with chosen stellar parameters, albeit with the dominant parameter affecting this variation being the chosen angle of inclination. Where there is a large uncertainty in the measured ($d\Omega$, Ω_{eq}), such as in the May 2011 and January 2015 epochs, the combination of parameters can create significant variation.

As a derived inclination angle for τ Boötis which is very close to our chosen value with a low level of uncertainty is known (cf. $44.5^\circ \pm 1.5^\circ$ (Brogi et al. 2012) vs 45°), the variation of inclination in our process by $\pm 10^\circ$ is somewhat conservative and thus our variation values may be overestimated. Consequently, we have a reasonable confidence that epoch-to-epoch changes in the field topology are real irrespective of the sometimes large and conservative variation measurements.

As with determining differential rotation, phase coverage must be adequate to successfully reconstruct the features on the stellar surface. Features, and thus energy in the harmonics may be missed if parts of the stellar surface are not observed. It is noted that the cadence observations of τ Boötis in observations after 2011 is lower than previous epochs. Consequently fewer phases are used in most of the epochs in this work compared to those of Donati et al. (2008) and Fares et al. (2009, 2013). Reconstruction of maps in this work with partial, sampled data sets shows that the latitude information of features and the overall field configurations

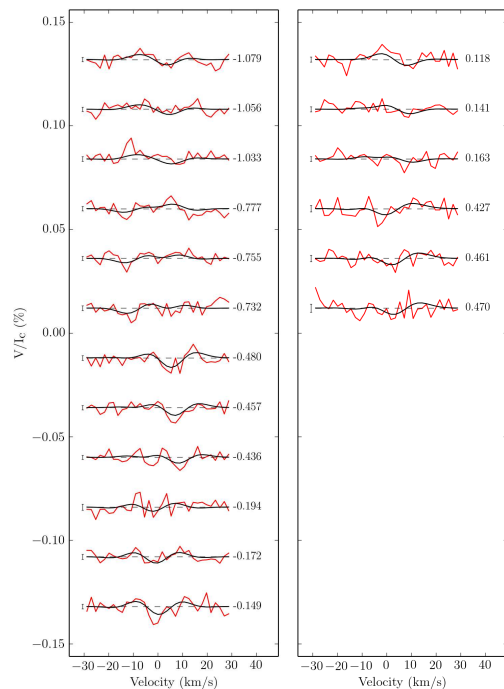


Figure 5. Circular polarization profiles of τ Boo for HARPSpol observations, May 2011. The observed profiles are shown in red, while synthetic profiles are shown in black. On the left of each profile we show a $\pm 1\sigma$ error bar. The rotational cycle of each observation is indicated on the right of each profile. All images of profile fits such as this are on the same scale across this work.

seem to be conserved, albeit with a reduction in the overall energy seen in the harmonics. These effects for a star with a weak magnetic field was discussed briefly by Fares et al. (2012) and is being further investigated in a forthcoming paper from Mengel et. al.

4.3.2 Results - HARPSpol - May 2011

Figure 5 shows the observed and reconstructed profiles for May 2011. Compared to the other epochs presented in this work, the magnetic signature is very small, and the observed profiles (in red) are relatively noisy, thus the reconstructed profiles begin fitting to the noise at a relatively high χ_r^2 . While HARPSpol has a higher resolution than NARVAL (110000 cf. 65000), the spectral coverage is smaller and consequently there are significantly fewer spectral lines to use in LSD. Nevertheless we observe, as per Fares et al. (2009), Fares et al. (2013), and Donati et al. (2008), that a weak magnetic field is manifest on the surface of τ Boötis in the order of 5 G to 10 G. The magnetic topology for May 2011 is shown in Fig. 7, top row. This topology was reconstructed with $\chi_r^2 = 1.10$.

The magnetic field has evolved in configuration from the January 2011 observation presented in Fares et al. (2013). The mean field is somewhat weaker at 2.2 G (although as noted before, a direct comparison of the HARPSpol B_{mod} may be of limited utility given the differences in the χ_r^2), and the percentage of the toroidal component of the field has remained around the same (from 18 to 20 percent). In addition, the field configuration has become more complex,

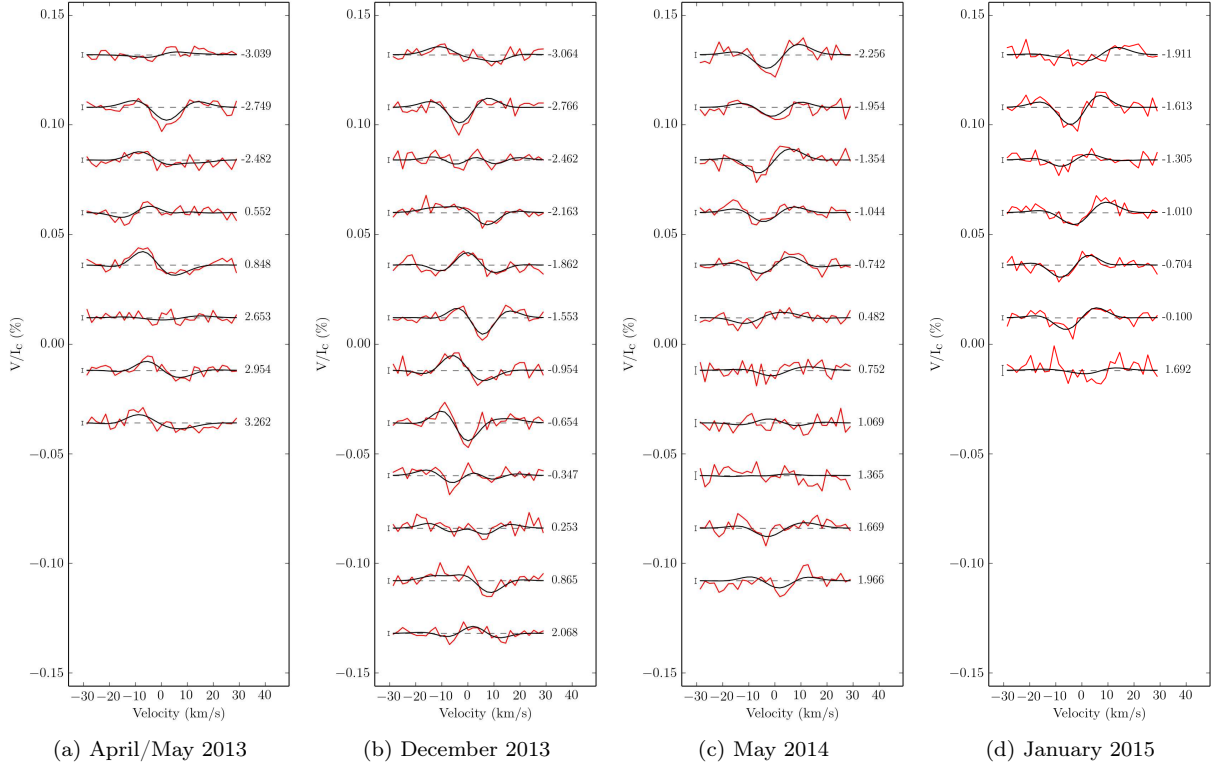


Figure 6. Circular polarization profiles of τ Boo for NARVAL observations, April 2013 through January 2015. The observed profiles are shown in red, while synthetic profiles are shown in black. On the left of each profile we show a $\pm 1\sigma$ error bar. The rotational cycle of each observation is indicated on the right of each profile.

with 19 percent ($m = 0$; value is ~ 25 percent if using $m = \ell/2$) of the poloidal component in an axisymmetric configuration compared to 37 percent, and only 26 percent of the poloidal component contained in modes $\ell \leq 2$ compared with 35 percent.

4.3.3 Results - NARVAL - April/May 2013 through January 2015

Over a period from April 2013 until January 2015, four epochs of τ Boötis were observed using NARVAL at TBL. The reconstructed (black) and observed (red) magnetic profiles for these epochs are shown in Fig. 6 (a), (b), (c) and (d). In all four epochs, magnetic signatures are clearly observed, and the evolution of the signatures with rotation is clear.

All three sets of maps were reconstructed using the same inclination and $v \sin i$ parameters and $\chi_r^2 = 0.95$. The values of the differential rotation parameters (Ω_{eq} , $d\Omega$) as derived in Section 4.2 for each epoch were used for each reconstruction.

It is clear from the maps (Fig. 7, second, third, fourth and bottom rows) and from the parameters of the magnetic topology that the large-scale magnetic field on τ Boötis evolved significantly over the eighteen month period.

Between April/May 2013 and December 2013, the field strength increased, and there was a negligible increase in the percentage of the calculated toroidal component. The amount of poloidal axisymmetry and the amount of field with

modes of $\ell \leq 2$ decreased (Table 6). In short, the field increased slightly in complexity.

Between December 2013 and May 2014, a significant change occurred with a clear reversal of polarity in the radial field, coincident with a significant decrease in the percentage of the toroidal component (24% to 13%), an increase in the axisymmetric poloidal component (30% to 46%) and a slight increase (40% to 45%) in the amount of the poloidal field with modes of $\ell \leq 2$. After the reversal, the field became more poloidal and symmetric.

Between May 2014 and January 2015 as the next polarity reversal (expected between January and May 2015) approached, the toroidal component of the field once more increased (from 12% to 30%), the axisymmetric component of the poloidal field dropped from 46 percent to 37 percent and the percentage of poloidal field in modes $\ell \leq 2$ decreased slightly from 45 to 41. This represents another increase in the complexity of the field as the radial field reversal approaches.

There have now been three sets of sequential epochs of τ Boötis observations which fall between radial field reversals. The latest two epoch pairs (April/May and December 2013; May 2014 and January 2015) presented in this work show an increase in field strength and in complexity between the reversals based on the amount of poloidal axisymmetric modes, modes with $\ell \leq 2$ and an increase in toroidal field. The other inter-reversal epoch pair (May 2009/January 2010; Fares et al. (2013)) of epochs showed an increase in field strength and a decrease in axisymmetry of the poloidal

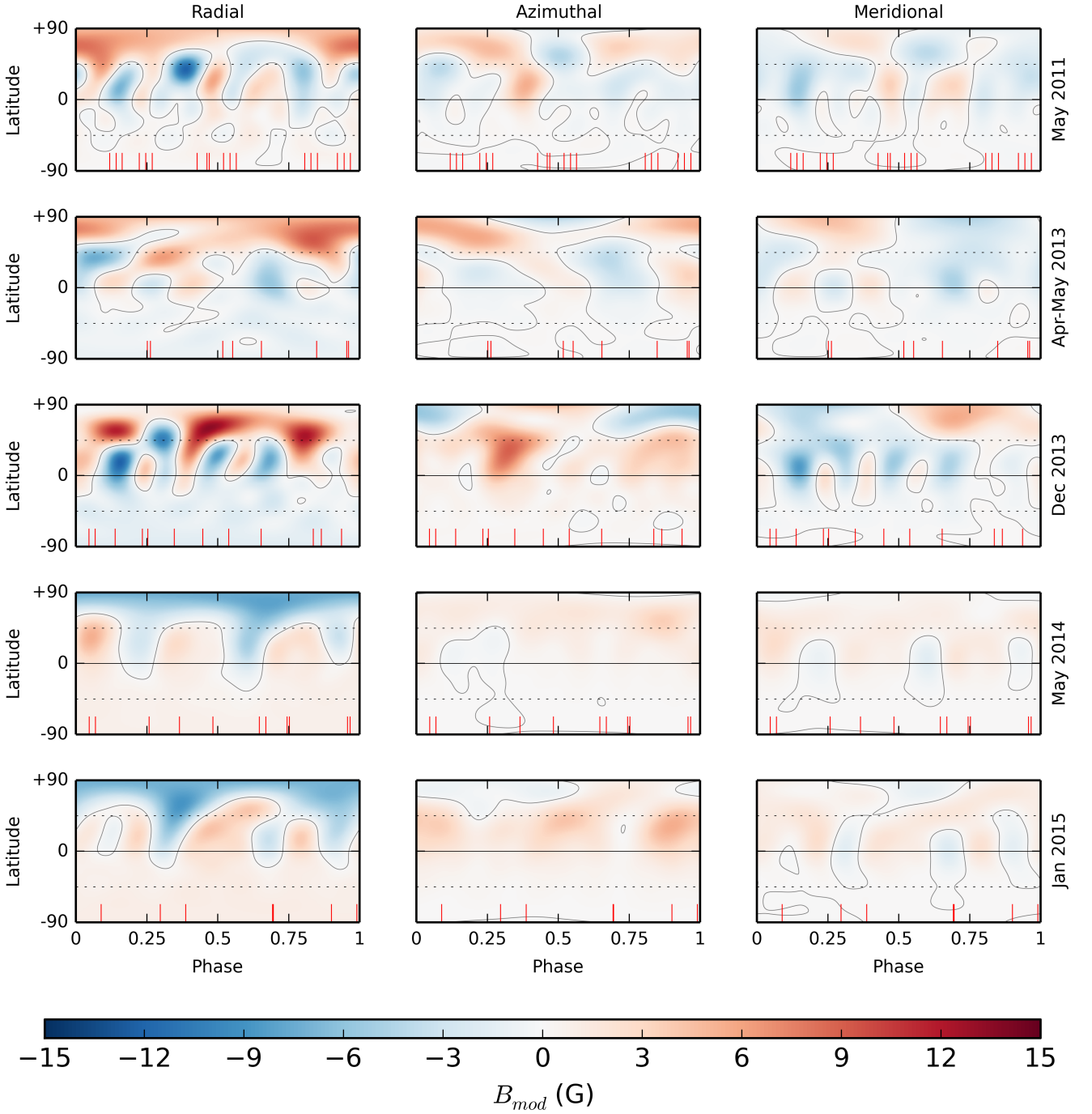


Figure 7. Magnetic topology of τ Boötis reconstructed from profiles in Fig. 5 and Fig. 6 (a) through (d). The radial, azimuthal and meridional components of the field (with magnetic field strength labelled in G) are depicted for May 2011 (top), April-May 2013 (second row), December 2013 (third row), May 2014 (fourth row), and January 2015 (bottom row). The contour line indicates where B_{mod} is zero. The red ticks along the lower x-axes indicate the observational phases for each epoch.

field however the percentage of toroidal field did not increase in that case.

4.3.4 Results - NARVAL - March through May 2015

Observations of τ Boötis from March until May 2015 presented a challenge for mapping as the data was very sparse

and spread over 70 d which corresponds to over 20 stellar rotations. This presents a problem due to the potential for feature evolution. In addition, only one or two observations per rotation leaves little information for determining differential rotation using the χ^2 -landscape technique.

The initial three observations (12-17 March 2015) were widely separated from the rest of the data set. A crude anal-

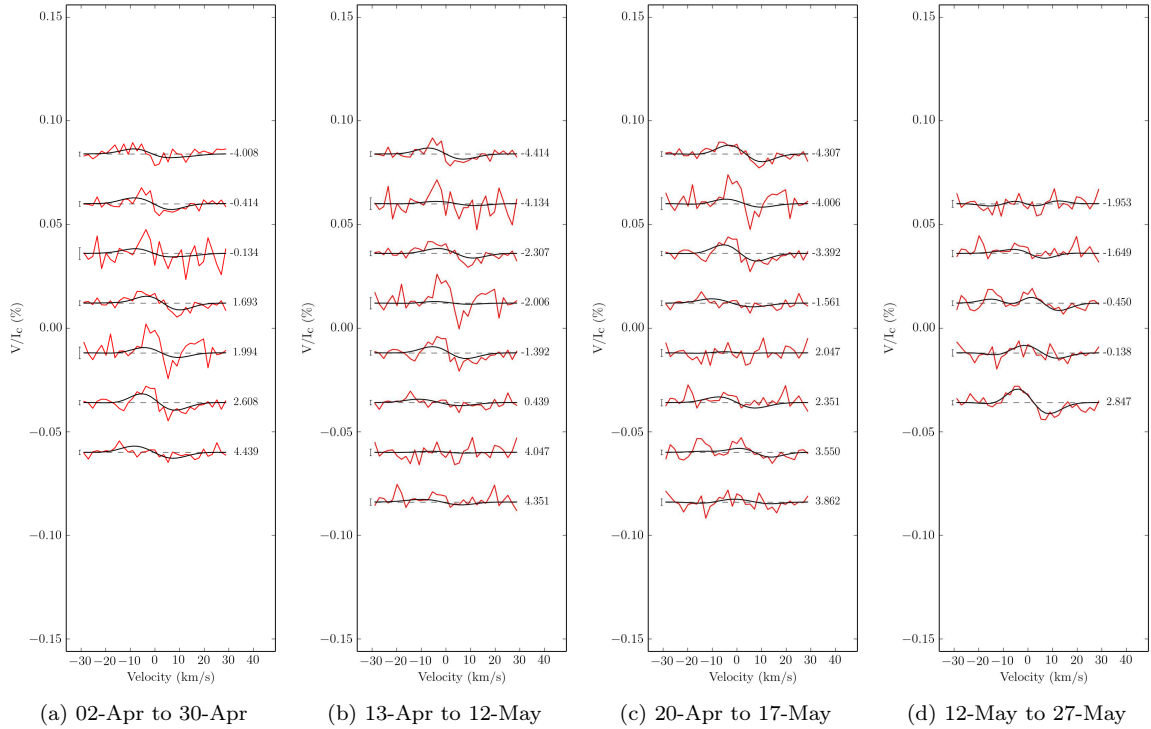


Figure 8. Circular polarization profiles of τ Boo from NARVAL April-May 2015. As shown in Table 4, four maps utilising a "sliding window" of approximately 8 rotations were used (apart from the final set of 5 rotations. The sets overlap and phases are as per Table 4. The observed profiles are shown in red, while synthetic profiles are shown in black. On the left of each profile we show a $\pm 1\sigma$ error bar. The rotational cycle of each observation is indicated on the right of each profile.

ysis using these three observations confirmed that the expected polarity reversal had occurred, meaning that it had occurred between late January and early March. The long time base of the March through May 2015 observations presented an opportunity to investigate this activity proxy minimum using the available data.

Utilising a sliding window of approximately 8 stellar rotations, the observations from April 2 through May 27 were split into four overlapping data sets (Fig. 10; Table 4) and maps were generated. Individual differential rotation measurements were made for each of the four data sets and the measurements are summarised in Table 5. As can be seen, the $d\Omega$ values were near solid-body and poorly-defined for the first three data sets. This is probably due to insufficient data for the technique (Morgenthaler et al. 2012). For each map, χ_r^2 of 0.95 was used.

The maps for the four data sets are shown in Figure 9 and the resulting field configuration information is presented in Table 7. While the sparseness of the data over this period and other observational biases such as poor S/N may contribute to the lack of features, if accurate, these maps show an intriguing progression through the activity proxy minimum. The observable field strength decreases as the minimum in S-index is passed and increases dramatically as the S-index begins to rise. In all cases, the strength is less than that from the January 2015 epoch prior to the dipole reversal despite being at a higher S-index.

Figure 10 does show there are several observations in this epoch that suffer from comparatively poor signal-to-

noise (circles $S/N < 1000$), where no magnetic signature is detected, which has an effect on the reconstruction. In contrast, the January 2015 data (Fig. 10; data located at \sim HJD 2457030) where the measured S-indices are lower than the March-May data, apart from the final observation, the data is excellent with S/N above 1386. Apart from the lowest S-index measurement, there are detections; mostly classified as definite. Thus it may appear at first glance that the variation in the S-index may not correlate with the level of magnetic activity we detect with ZDI due to the effects of varying data quality.

However, if we ignore the March-May 2015 observations with $S/N < 1000$, a pattern does appear where as the S-index decreases, the magnetic detections become marginal until finally there is a non-detection. Further, examining all of the observations from the NARVAL epochs presented in this paper (Fig. 11, excluding $S/N < 1150$ where there is only a single marginal detection), it is clear that as the quality of the data improves, the proportion of marginal detections decreases, while non-detections only appear at lower S-indices. Hence while the data quality is a factor, it is possible to say that chromospheric activity does exhibit a relationship to the observed magnetic activity of τ Boötis.

This may only be within a particular chromospheric activity cycle. Noting that although the S-indices for January 2015 were universally lower than March-May 2015, the star's magnetic field was stronger in January. This may mean that there is a *general* increase in magnetic activity as the star's magnetic cycle proceeds from one reversal to the next, while

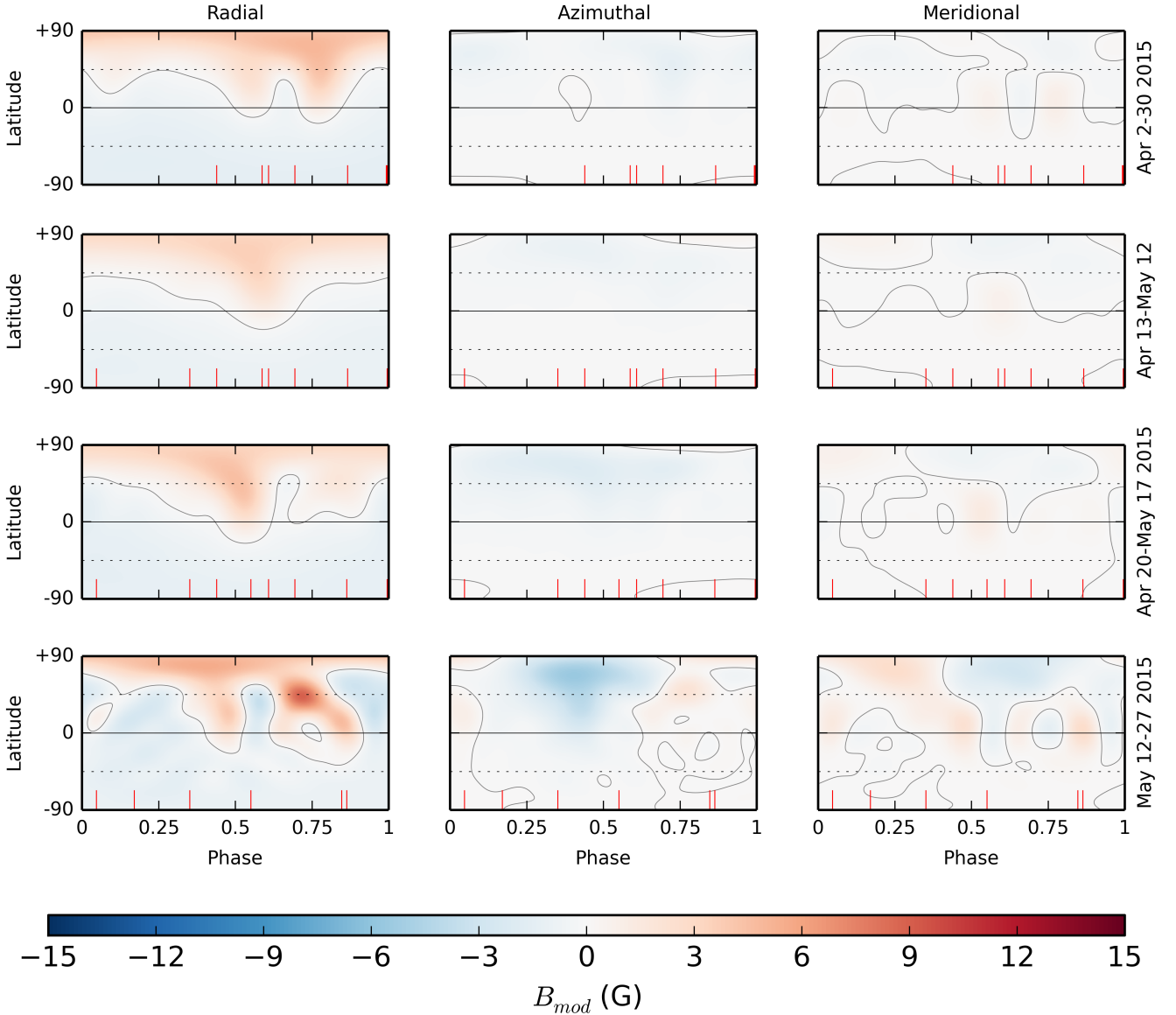


Figure 9. Magnetic topology of τ Boötis reconstructed from profiles in Fig. 8 (a) through (d). The radial, azimuthal and meridional components of the field (with magnetic field strength labelled in G) are depicted. The contour line indicates where B_{mod} is zero. The red ticks along the lower x-axes indicate the observational phases for each epoch.

there is a smaller modulation following the chromospheric activity cycle of which there appear to be ~ 3 per intra-reversal period ($\sim 117\text{d} \sim 1\text{yr}$). However, the existing data is not detailed enough to make this statement definitively. Indeed, examining previous epochs and given the uncertainty in exactly when the polarity reversal occurs, it is possible to speculate that the magnetic cycle may correspond to the chromospheric cycle. Three reversals per year would potentially manifest as a yearly reversal due to observational cadences. This is discussed further in Section 5.

The field configuration for March-May 2015 appears to be generally highly symmetrical for the first three data sets, however there is very little energy in the spherical harmonics to work with during the S-index minimum. It is clear though that after the minimum, there is noticeably more toroidal field evident, and a significant decrease in poloidal

axisymmetry and dipolar/quadrupolar modes. This result further suggests that a magnetic activity cycle appears to be coincident with the chromospheric activity cycle.

Given that $\phi_{rot} = 0$ is synchronised in each map, it is possible to see features migrating across the star between March and May 2015, probably due to differential rotation. In addition, in the final two data sets, the emergence of the prominent feature at $+45^\circ$ near $\phi_{rot} = 0.75$ with time is clear. While this may be due to observational effects, it also may be due to increased intensity leading to feature evolution. Notably, maps 1, 3 and 4 all exhibit active regions near $\phi_{rot} = 0.75$. Coincidentally, this is near the active longitude suggested by Shkolnik et al. (2008).

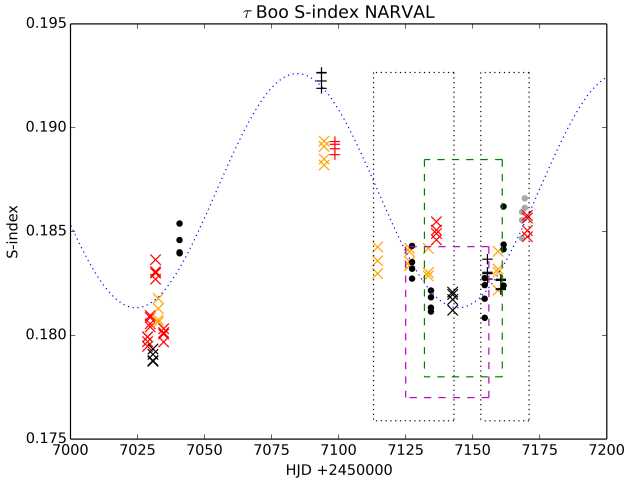


Figure 10. Ca II HK S-indices for τ Boötis for January (~ 7030 HJD+2450000) through May 2015. NARVAL observations are shown as follows: red = definite detection; orange = marginal detection; black = no detection; grey = incomplete Stokes V sequence. Marker shapes represent S/N near ~ 700 nm in the Stokes V spectrum: circles = $S/N < 1000$; + = $1000 < S/N < 1300$; \times = $S/N > 1300$. A least-squares fit to the unweighted data (blue line) yields a period of ~ 120 d, similar to that reported in [Baliunas et al. \(1997\)](#). The leftmost black dotted rectangle indicates the observations used for the profiles in Figure 8(a). The magenta and green dashed rectangles correspond to Figure 8(b) and (c) respectively. The rightmost dotted rectangle indicates the observations used for the profiles in Figure 8(d).

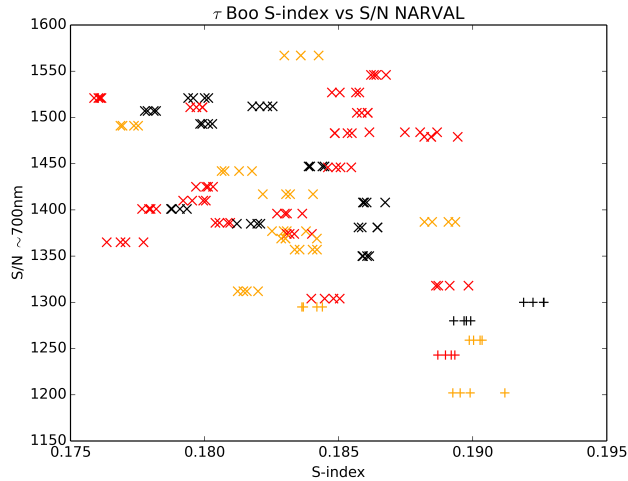


Figure 11. Signal to Noise measured at ~ 700 nm in the Stokes V spectra plotted against Ca II HK S-indices for τ Boötis for all NARVAL observations presented in this paper. Observations are shown as follows: red = definite detection; orange = marginal detection; black = no detection. Marker shapes represent S/N near ~ 700 nm in the Stokes V profile: + = $1000 < S/N < 1300$; \times = $S/N > 1300$. There is only one marginal detection below $SN \approx 1100$; all others are non-detections. These observations excluded for clarity.

Table 4. Use of exposures from April and May 2015 (Table B3) and their use in each map reconstruction. The rotational cycle used for calculating 0.0 (from Equation 1) is shown for each map. (* - Observation on 19-May with very poor S/N was not used in the reconstruction)

Obs.	Cycle	Map 1 ϕ_{rot}	Map 2 ϕ_{rot}	Map 3 ϕ_{rot}	Map 4 ϕ_{rot}
02-Apr-2015	1105.992	-4.008			
13-Apr-2015	1109.586	-0.414	-4.414		
14-Apr-2015	1109.866	-0.134	-4.134		
20-Apr-2015	1111.693	1.693	-2.307	-4.307	
21-Apr-2015	1111.994	1.994	-2.006	-4.006	
23-Apr-2015	1112.608	2.608	-1.392	-3.392	
30-Apr-2015	1114.439	4.439	0.439	-1.561	
11-May-2015	1118.047		4.047	2.047	-1.953
12-May-2015	1118.351		4.351	2.351	-1.649
16-May-2015	1119.550			3.550	-0.450
17-May-2015	1119.862			3.862	-0.138
19-May-2015	1120.170				*
27-May-2015	1122.847				2.847
$\phi_{rot} = 0$ Cycle		1110	1114	1116	1120

Table 5. Summary of measured differential rotation parameters for τ Boötis for the four maps March through May 2015. Note the anti-solar $d\Omega$ for the first three epochs, due to poor coverage and/or low detectability of the magnetic field.

Epoch	Ω_{eq} rad d $^{-1}$	$d\Omega$ rad d $^{-1}$
2015 02 Apr - 30 Apr	$2.01^{+0.01}_{-0.15}$	$-0.07^{+0.07}_{-0.04}$
2015 13 Apr - 12 May	$1.88^{+0.15}_{-0.04}$	$-0.12^{+0.13}_{-0.09}$
2015 20 Apr - 17 May	$1.93^{+0.01}_{-0.01}$	$-0.04^{+0.04}_{-0.03}$
2015 12 May - 27 May	$1.92^{+0.02}_{-0.06}$	$+0.17^{+0.16}_{-0.14}$

5 DISCUSSION AND CONCLUSIONS

The March through May 2015 observational epoch makes clear that τ Boötis is near the limit of our ability to apply ZDI. A small magnetic survey of ~ 20 planet hosting stars utilising NARVAL (Mengel et. al., in preparation) and the wider BCool survey ([Marsden et al. 2014](#)) finds that fainter stars (these surveys are to $V \sim 9$) with an S-index less than ~ 0.2 usually have magnetic fields too weak to detect. τ Boötis is thus unusual in this regard, due to its brightness ($V \approx 4.5$) compared to the wider sample allowing for adequate signal-to-noise for ZDI. When τ Boötis is at the nadir of its chromospheric activity cycle, the magnetic field is on the very limit of where NARVAL can with confidence detect the Zeeman signature.

Despite this limitation, the evolution of the large-scale magnetic field of τ Boötis is apparent in the results we present here over two timescales and (what appear to be) two cyclic periods. Most significantly, τ Boötis appears to undergo polarity switches on a regular basis. [Fares et al. \(2013\)](#) notes that the polarity switch appears to be a phenomenon occurring every 360 d, and these latest observations would seem to confirm this hypothesis. The regular reversals appear to occur between January and March in each calendar year. Additionally, magnetic energy appears

to rise and fall in a shorter cycle coincident with the S-index of the star.

The evolution of the magnetic field during the period between reversals is illuminating insofar as the behaviour of the large scale field broadly follows what one would expect in a star such as the Sun. In Fig. 15, the fractional magnetic field for each of the three components at each latitude is shown for these three epochs. Between April/May 2013 and December 2013, the intensity of the radial and azimuthal components increases and the latitude at which the peak intensity is observed decreases towards the equator (Fig 15 (a) and (b)). After the polarity switch, the radial and azimuthal fields have a relatively lower intensity and their peak intensity is at latitudes close to the pole (Fig. 15 (c)). This cycle then repeats between the two observed radial field reversals (Fig. 12). This pattern of intensifying azimuthal field at lower latitudes approaching a reversal was observed between May 2009 and January 2010, the only similar set of observations taken between a pair of reversals. It should be noted that with poorer phase coverage, the potential uncertainty in the latitudes of recovered features increases, particularly in the azimuthal and meridional components. This is because with sparser phase coverage, we are less likely to observe either the exact points of entry or exit (or indeed both) of features on the visible stellar surface. The level of this uncertainty is difficult to characterise, thus further observations with higher cadence and denser phase coverage may be required to absolutely confirm the nature of the latitudinal migration of features we propose here.

As a polarity shift approaches, the field also becomes less axisymmetric in the poloidal component and more complex, with slightly less of the poloidal field in modes corresponding to dipolar and quadrupolar components. After the polarity shift occurs, the amount of the toroidal field decreases significantly and the field becomes simpler; more axisymmetric and more strongly dipolar/quadrupolar. (Note that between May 2009 and January 2010 (Fares et al. 2013), the percentage of axisymmetric modes similarly dropped precipitously, however, the complexity of the field decreased slightly differing from the 2013 epochs).

The ~ 117 d period of the Ca II H&K index coupled with a posited \sim yearly radial field polarity reversal suggests a 3:1 periodic relationship between the cycles. Reversals appear to occur at or near the peak of every third chromospheric cycle. While the sequence of maps by Fares et al. (2009, 2013); Donati et al. (2008); Catala et al. (2007) indicates that the period of reversal appear to be yearly, this may not necessarily be the case. On the face of it, τ Boötis has an approximately 720 d magnetic cycle, which is mostly, but not completely, an analogue of a solar-like cycle. Our results from March through May 2015 show that the timing of the observational epochs for τ Boötis may in fact disguise a much faster cycle, such as the 240 d period found by Fares et al. (2013).

Figure 13 presents the magnetic field configuration information from Tables 6 and 7, also showing the location of the approximate date of the magnetic polarity reversal. The rapid change in the activity during March through May 2015 would seem to suggest that the magnetic activity cycle is coincident with the chromospheric activity cycle of τ Boötis. Were reversals coincident with the peak of the chromospheric activity cycle, the similarity of the 2013 though

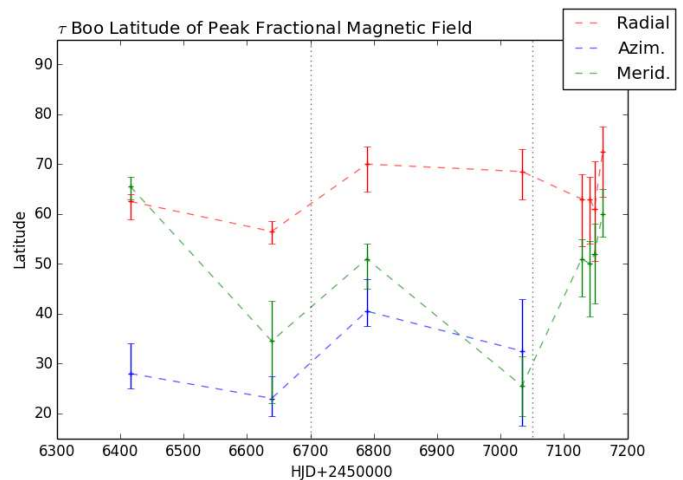


Figure 12. Latitude of peak fractional magnetic field components for epochs April-May 2013 through January 2015 with variation bars from Figure 15 and for the March through May 2015 epoch. The black dotted lines indicate a radial field reversal has taken place. Azimuthal field is not included for the March though May 2015 epoch for clarity as the small amount of azimuthal field is spread across a wide area, making the variation bars extremely large.

January 2015 results would appear to be more related to the similarity their position in the chromospheric cycle more than any intrinsic variation between reversals. Figure 12 also shows that the decrease in peak fractional latitude (interpreted as solar-like behavior above) is reversed in the March-May 2015 epoch. This is perhaps due to the strengthening of the polar features in conjunction with the overall magnetic field (Fig. 14, and it would be interesting to see if the peak fractional latitude began to decrease as the chromospheric cycle continued).

Examining previous published results, no reversal between January and June 2008 would appear to settle the matter of a yearly reversal. However, given the large gap in observations between regular observations in 2008 and 2013 and the fact that three times the observational period is not exactly a year, the approximate time of the reversal may have drifted. It is possible two reversals may have occurred in the period between January and June 2008. Further spectropolarimetric observations of τ Boötis during each of the three ~ 117 d chromospheric cycles would be required to confirm the periodicity of the polarity reversal. If the reversals are confirmed to be on a yearly basis, then a mechanism whereby the 3:1 relationship between chromospheric activity and magnetic activity would need to be posited. Magnetohydrodynamic simulations of dynamo and convective processes in F-type stars by Augustson et al. (2013) shows magnetic energy rising and falling regularly with a magnetic reversal occurring on the third such magnetic cycle thus potentially providing such a mechanism.

Our conclusions about the behaviour of τ Boötis should not be significantly altered were the reversal shown to be shorter. As our March through May 2015 observations show, the broad solar-like behaviour of the magnetic field of τ Boötis should still be present, simply on a shorter timescale.

Irrespective of future work on determining the rever-

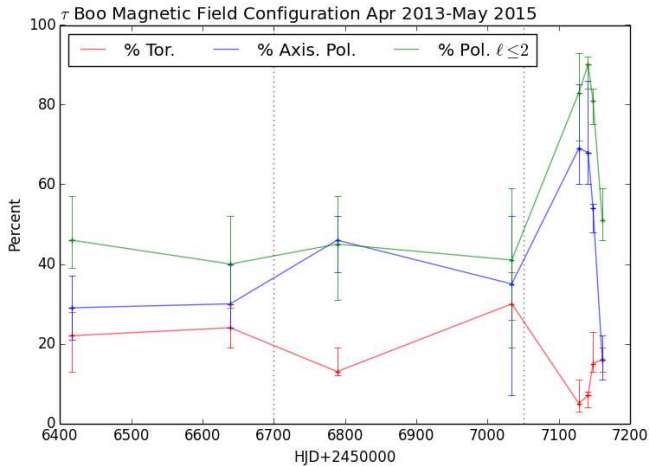


Figure 13. Plot of magnetic field topology from Tables 6 and 7. The black dotted lines indicate approximately where a radial field reversal has taken place. The rapid evolution of the measured field components after HJD 2457100 (Mar-May 2015) is coincident with the chromospheric cycle and suggests the magnetic cycle may be more rapid than the ~ 720 d cycle previously assumed.

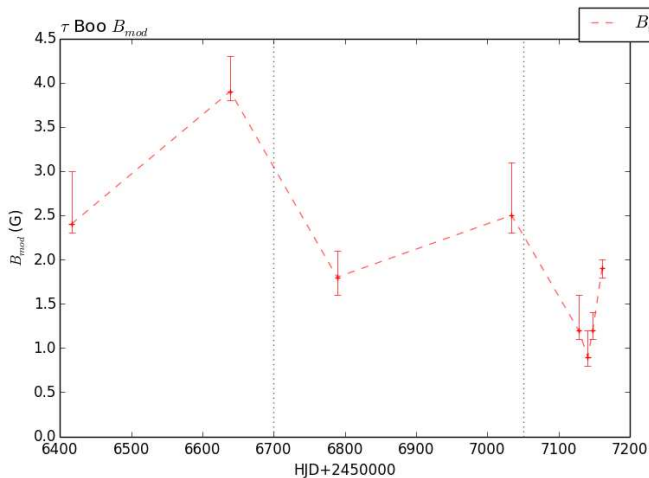


Figure 14. Plot of mean magnetic field strength (B_{mod}) from Tables 6 and 7. The black dotted lines indicate approximately where a radial field reversal has taken place.

sal cycle, an observational campaign such as March through May 2015 which spanned the maximum of the chromospheric activity would be very interesting, especially during the period of the magnetic reversal. This would provide insights into the evolution of the magnetic field leading up to, during and following a reversal.

Borsa et al. (2015) performed observations of τ Boötis in April-May 2013 which were coincident with the April-May 2013 epoch presented in this work. Unfortunately, while they observe a plage at high latitude near $\phi_{rot} \approx 0.1$, our observations did not provide any coverage centred on that phase. However, we do see a strong polar/high latitude magnetic feature covering $\phi_{rot} \approx 0.85$ to $\phi_{rot} \approx 0.0$. Given the lack

of phase-coincident observations, we cannot confirm or rule out a bright spot observed by Borsa et al. (2015).

While casual observation of the maps we present in this work seem to consistently show a feature present near $\phi_{rot} \approx 0.8$, potentially coincident with the bright spot posited by Walker et al. (2008), analysis of all of the data does not reliably show a persistent active longitude. However, not every data set has coverage of this phase, and those that do may only have one or two observations over several rotations. Thus we can neither rule out nor confirm if there are magnetic features potentially induced by SPI or other means.

In summary, τ Boötis is a prime candidate for further investigation. It exhibits a complex interplay of chromospheric and magnetic cycles. Whether the hot Jupiter orbiting the star is affecting these cycles is inconclusive, however further observations may be able to provide more compelling information in the future.

ACKNOWLEDGMENTS

This work was based on observations obtained with HARPSpol at the ESO 3.6-m telescope at La Silla and with NARVAL at the Telescope Bernard Lyot (TBL). TBL/NARVAL are operated by INSU/CNRS. Previous spectropolarimetric observations of τ Boötis were obtained from the Polarbase repository of EsPaDOs and NARVAL observations. In particular we thank the BCool Collaboration for providing time in their long-term program for ongoing observations of τ Boötis.

SVJ acknowledges research funding by the Deutsche Forschungsgemeinschaft (DFG) under grant SFB 963/1, project A16. CPF is supported by the grant ANR 2011 Blanc SIMI5-6 020 01 “Toupiques: Towards understanding the spin evolution of stars”.

The Strategic Research Funding for the Starwinds project provided by the University of Southern Queensland provides resources to the Astrophysics group within the Computational Engineering and Science Research Centre at USQ (MWM, SCM, BDC). MWM is supported by an Australian Postgraduate Award Scholarship.

We thank Claude Catala and Monica Rainer for their assistance in the development of the FT differential code produced by MWM for use in this paper.

Iterative calculations for differential rotation were performed using the University of Southern Queensland High Performance Computing cluster. We thank Richard Young for his assistance in utilising the HPC resources at USQ.

This research has made use of NASA’s Astrophysics Data System.

REFERENCES

- Augustson K. C., Brun A. S., Toomre J., 2013, *ApJ*, 777, 153
- Aurière M., 2003, in Arnaud J., Meunier N., eds, *EAS Pub. Ser. Vol. 9, Magnetism and Activity of the Sun and Stars*. p. 105
- Baliunas S. L., Henry G. W., Donahue R. A., Fekel F. C., Soon W. H., 1997, *ApJ*, 474, L119
- Baliunas S. L., Donahue R. A., Soon W. H., Henry G. W., 1998, in Donahue R. A., Bookbinder J. A., eds, *ASP Conf. Ser. Vol.*

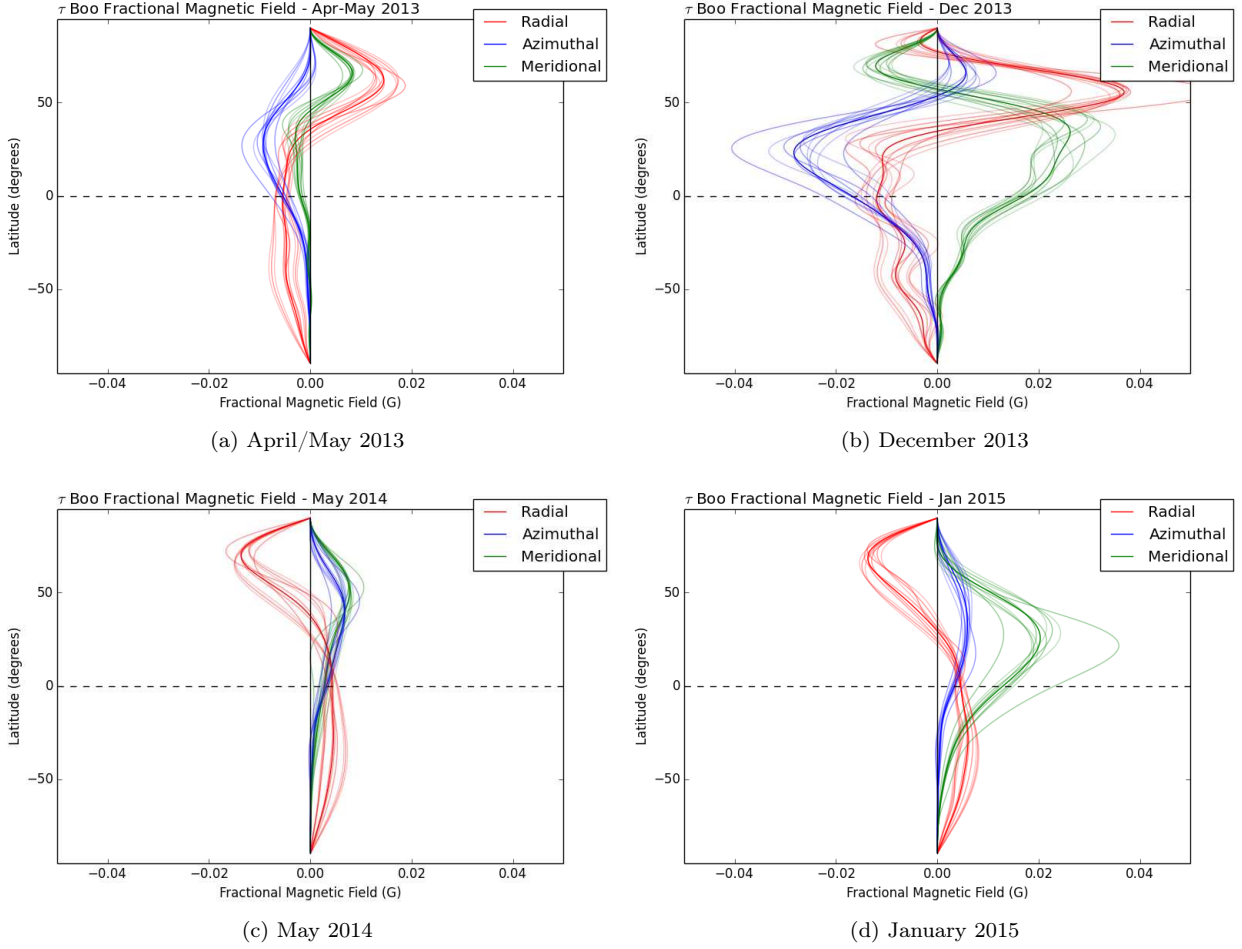


Figure 15. Fractional magnetic field by latitude for (a) April/May 2013, (b) December 2013, (c) May 2014, and (d) January 2015. The radial component is shown in red, azimuthal component in blue, and meridional component in green. Solid dark lines represent the result using the parameters used for mapping (inclination 45° , $v \sin i$ 15.9 km s^{-1}). Shaded areas represent varying inclination $\pm 10^\circ$ and $v \sin i \pm 1 \text{ km s}^{-1}$. The reversal in the radial field is evident between December 2013 and May 2014. The peak intensity of the field components occur at slightly lower latitudes as the reversal approaches, then revert to higher latitudes after the reversal. It is noted that the above plots assume an annual magnetic field reversal (see further discussion in Section 5).

Table 6. Summary of magnetic topology evolution of τ Boötis 2011-2015. The columns indicated mean magnetic field B , percentage of magnetic energy in the toroidal component, percentage of the energy contained in the axisymmetric modes of the poloidal component (modes with $m = 0$) and percentage of the energy contained in the modes of $\ell \leq 2$ of the poloidal component. Variations are based on systematic recalculation based upon varying stellar parameters (Ω_{eq} , $d\Omega$, inclination, $v \sin i$) as described in Appendix A.

Epoch	B (G)	% toroidal	% axisymm. poloidal	% $\ell \leq 2$ in poloidal
2011 May	$2.5^{+0.4}_{-0.1}$	20^{+11}_{-5}	19^{+14}_{-6}	26^{+17}_{-7}
2013 April/May	$2.4^{+0.6}_{-0.1}$	22^{+6}_{-9}	29^{+8}_{-8}	46^{+11}_{-7}
2013 December	$3.9^{+0.4}_{-0.1}$	24^{+6}_{-5}	30^{+10}_{-6}	40^{+12}_{-11}
2014 May	$1.8^{+0.3}_{-0.2}$	13^{+6}_{-1}	46^{+6}_{-8}	45^{+12}_{-14}
2015 Jan	$2.5^{+0.6}_{-0.2}$	30^{+8}_{-4}	35^{+17}_{-28}	41^{+18}_{-22}
2015 March		see Table 7		

Table 7. Summary of magnetic topology evolution of τ Boötis for the four maps March through May 2014. The columns indicated mean magnetic field B , percentage of magnetic energy in the toroidal component, percentage of the energy contained in the axisymmetric modes of the poloidal component (modes with $m = 0$) and percentage of the energy contained in the modes of $\ell \leq 2$ of the poloidal component. Variations are based on the systematic recalculation based upon varying stellar parameters (Ω_{eq} , $d\Omega$, inclination, $v \sin i$) as described in Appendix A.

Epoch	B (G)	% toroidal	% axisymm. poloidal	% $\ell \leq 2$ in poloidal
2015 02 Apr - 30 Apr	$1.2^{+0.4}_{-0.1}$	5^{+6}_{-2}	69^{+16}_{-9}	83^{+10}_{-12}
2015 13 Apr - 12 May	$0.9^{+0.3}_{-0.1}$	7^{+1}_{-3}	68^{+18}_{-8}	90^{+2}_{-6}
2015 20 Apr - 17 May	$1.2^{+0.2}_{-0.1}$	15^{+8}_{-2}	54^{+1}_{-6}	81^{+3}_{-6}
2015 12 May - 27 May	$1.9^{+0.1}_{-0.1}$	16^{+3}_{-3}	16^{+6}_{-5}	51^{+8}_{-5}

154, Cool Stars, Stellar Systems and the Sun. Astron. Soc. of the Pac., pp 153–172

Borsa F., et al., 2015, A&A, 578, 64

Broggi M., Snellen I. A. G., de Kok R. J., Albrecht S., Birkby J., de Mooij E. J. W., 2012, Nature, 486, 502

Butler R. P., Marcy G., Williams E., Hauser H., Shirts P., 1997, ApJ, 474, L115

Catala C., Donati J.-F., Shkolnik E., Bohlender D., Alecian E., 2007, MNRAS, 374, L42

Donati J.-F., 2003, in Trujillo-Beuno J., Almeida J. S., eds, ASP Conf. Ser. Vol. 307, Solar Polarization 3. Astron. Soc. of the Pac., San Francisco, p. 41

Donati J.-F., Semel M., Carter B. D., Rees D. E., Collier Cameron A., 1997, MNRAS, 291, 658

Donati J.-F., Mengel M., Carter B. D., Marsden S., Collier Cameron a., Wichmann R., 2000, MNRAS, 316, 699

Donati J.-F., Cameron A., Petit P., 2003, MNRAS, 345, 1187

Donati J.-F., et al., 2006, MNRAS, 370, 629

Donati J.-F., et al., 2008, MNRAS, 385, 1179

Fares R., et al., 2009, MNRAS, 398, 1383

Fares R., et al., 2012, MNRAS, 423, 1006

Fares R., Moutou C., Donati J.-F., Catala C., Shkolnik E. L., Jardine M. M., Cameron A. C., Deleuil M., 2013, MNRAS, 435, 1451

Henry G. W., Baliunas S. L., Donahue R. A., Fekel F. C., Soon W., 2000, ApJ, 531, 415

Jeffers S. V., Donati J.-F., 2008, MNRAS, 390, 635

Jeffers S. V., Donati J.-F., Alecian E., Marsden S. C., 2011, MNRAS, 411, 1301

Lanza A. F., 2012, A&A, 544, AA23

Leigh C., Cameron A., Horne K., Penny A., James D., 2003, MNRAS, 344, 1271

Marsden S., Donati J.-F., Semel M., Petit P., Carter B., 2006, MNRAS, 370, 468

Marsden S. C., et al., 2014, MNRAS, 444, 3517

Mayor M., et al., 2003, The Messenger, 114, 20

Morgenthaler a., et al., 2012, A&A, 540, A138

Morin J., et al., 2008, MNRAS, 384, 77

Morin J., Donati J.-F., Petit P., Delfosse X., Forveille T., Jardine M. M., 2010, MNRAS, 407, 2269

Nicholson B. A., et al., 2016, MNRAS, submitted

Petit P., Donati J.-F., Collier-Cameron A., 2002, MNRAS, 334, 374

Petit P., Louge T., Thêado S., Paletou F., Manset N., Morin J., Marsden S. C., Jeffers S. V., 2014, PASP, 126, 469

Piskunov N., et al., 2011, The Messenger, 143, 7

Reiners A., 2006, A&A, 446, 267

Reiners A., Schmitt J. H. M. M., 2003, A&A, 398, 647

Rodler F., Lopez-Morales M., Ribas I., 2012, ApJ, 753, L25

Semel M., Donati J.-F., Rees D. E., 1993, A&A, 278, 231

Shkolnik E., Bohlender D. A., Walker G. A. H., Collier Cameron

A., 2008, ApJ, 676, 628

Vidotto A. A., Fares R., Jardine M., Donati J.-F., Opher M., Moutou C., Catala C., Gombosi T. I., 2012, MNRAS, 423, 3285

Walker G. A. H., et al., 2008, A&A, 482, 691

Wright J. T., Marcy G. W., Butler R. P., Vogt S. S., 2004, ApJS, 152, 261

APPENDIX A: DERIVING VARIATION MEASUREMENTS FOR MAGNETIC FIELD CONFIGURATION

As the energy in the spherical harmonics produced by the ZDI mapping process provide exact values for a given set of modes, a measure of variability of the field configuration values (Tables 6 and 7), due to the uncertainties in the stellar parameters, is desirable. We achieve this by varying the stellar parameters, re-running the mapping process and extracting the various parameters. As variation in $v \sin i$ and stellar inclination are used in determining the variation of the differential rotation parameters (Ω_{eq} , $d\Omega$) (see Fig. 3(b)), we hold each pair of parameters ($v \sin i$, inclination) and (Ω_{eq} , $d\Omega$) constant while varying the others. Otherwise we generate extreme variations where all parameters are varied to extremes.

Figure A1 shows a plot of the percentage of poloidal field modes $\ell \leq 2$ from the May 2014 data set where we vary (Ω_{eq} , $d\Omega$), holding ($v \sin i$, inclination) constant. Taking the $\sim 1\text{-}\sigma$ variation in (Ω_{eq} , $d\Omega$) from the measured value (shown as a yellow cross in Fig. A1; Tables 3 and 5 show variations used) gives us an indication of how the differential rotation measurement affects this field component.

Figure A2 similarly shows the effect on the measured field component of varying $v \sin i$ and inclination angle while holding the DR parameters steady at the measured values.

From these measurements, we take the extreme variations from both methods to provide the variations shown in Tables 6 and 7.

It is clear that the dominant parameter for variation of poloidal axisymmetry and dipolar/quadrupolar components is the stellar inclination angle we choose. This is as expected, as errors in the assumed inclination of the star's rotational axis will affect axisymmetry and latitudes of features. As we use a large variation in inclination ($\pm 10^\circ$), our derived variations in these values are systematically larger than those in the percentage of toroidal field and B_{mod} .

APPENDIX B: JOURNALS OF OBSERVATIONS

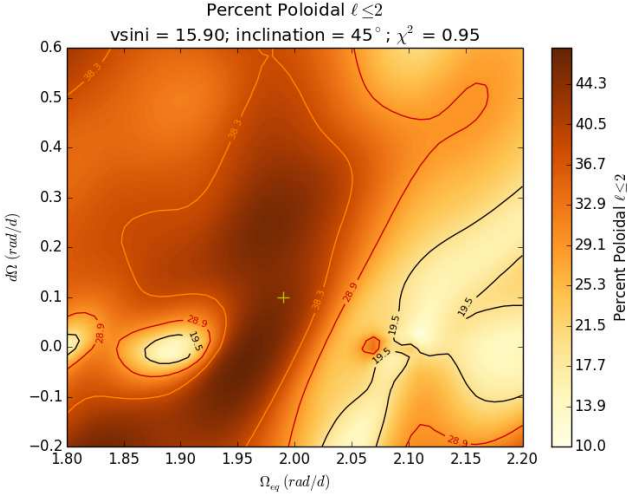


Figure A1. Plot of percentage of poloidal modes $\ell \leq 2$ varying Ω_{eq} and $d\Omega$ for the May 2014 data set, using the values of $v \sin i = 15 \text{ km s}^{-1}$ and inclination of 45° . The yellow cross indicates the measured differential rotation.

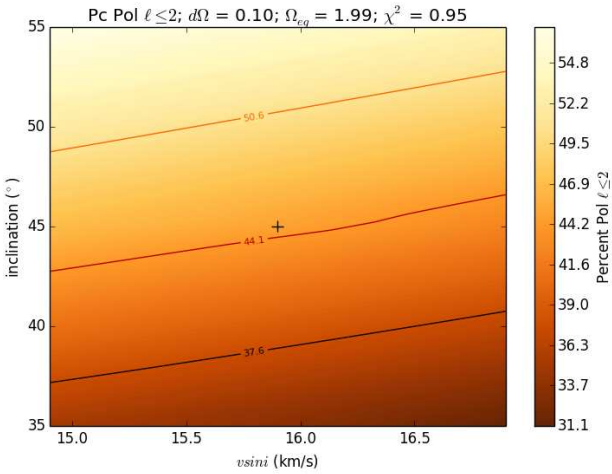


Figure A2. Plot of percentage of poloidal modes $\ell \leq 2$ varying $v \sin i$ and angle of inclination for the May 2014 data set, using the measured values for differential rotation. The black cross indicates the $v \sin i$ and inclination chosen for the nominal reconstruction via χ^2 minimization described in Section 4.

Extreme changes in Ω_{eq} are significant, but usually, this value is relatively well constrained. Extreme variation in $d\Omega$ can have an effect on the variation in the toroidal field component, but only if the variation is very large. If variation of $d\Omega$ is not significantly greater than the $\sim 1\text{-}\sigma$ variation in measured value, $d\Omega$ appears not to have a large effect on the field configuration parameters we derive.

In conclusion, we believe the field configuration parameters we derive are robust and stable, assuming the methodology we use is internally consistent using the derived parameters for $v \sin i$, inclination and differential rotation.

Table B1. Journal of HARPSpol observations of τ Boötis. Columns list the UT date, instrument used, the heliocentric Julian date (at midpoint of the series of 4 sub-exposures), the UT time (at midpoint of the series of 4 sub-exposures), the exposure time, the peak signal-to-noise ratio (SNR) of each observation (around 583 nm for HARPSpol observations), the rotational cycle from the ephemeris (from Equation 1), the rotational phase (0.0 being approximately the centre of the observing run), the radial velocity (RV) associated with each exposure, and whether a magnetic signature is detected (D; $fap < 10^{-5}$), marginally detected (M; $10^{-3} > fap > 10^{-5}$) or is below the detection threshold (N).

Date	Instrument	HJD (245 5000+)	UT (h:m:s)	T_{exp} (s)	SNR	Cycle	ϕ_{rot}	RV (km s^{-1})	Detection
15-May-2011	HARPSpol	696.57356	01:39:37	4×600	1081	677.921	-1.079	-16.613	N
15-May-2011	HARPSpol	696.65020	03:29:59	4×600	1101	677.945	-1.056	-16.544	N
15-May-2011	HARPSpol	696.72435	05:16:46	4×600	1025	677.967	-1.033	-16.483	N
16-May-2011	HARPSpol	697.57360	01:39:44	4×600	1074	678.223	-0.777	-15.919	M
16-May-2011	HARPSpol	697.64667	03:24:57	4×600	1149	678.245	-0.755	-15.909	N
16-May-2011	HARPSpol	697.72308	05:14:59	4×600	1117	678.268	-0.732	-15.914	N
17-May-2011	HARPSpol	698.55641	01:15:01	4×600	1052	678.520	-0.480	-16.455	M
17-May-2011	HARPSpol	698.63125	03:02:48	4×600	1065	678.543	-0.457	-16.520	N
17-May-2011	HARPSpol	698.70306	04:46:12	4×600	1124	678.564	-0.436	-16.574	M
17-May-2011	HARPSpol	699.50424	23:59:57	4×600	838	678.806	-0.194	-16.815	N
18-May-2011	HARPSpol	699.57741	01:45:19	4×600	1029	678.828	-0.172	-16.792	N
18-May-2011	HARPSpol	699.65246	03:33:24	4×600	1069	678.851	-0.149	-16.777	D
19-May-2011	HARPSpol	700.53841	00:49:12	4×600	970	679.118	0.118	-16.052	N
19-May-2011	HARPSpol	700.61374	02:37:41	4×600	964	679.141	0.141	-15.999	N
19-May-2011	HARPSpol	700.68619	04:22:01	4×600	998	679.163	0.163	-15.968	N
20-May-2011	HARPSpol	701.56019	01:20:38	4×600	778	679.427	0.427	-16.183	N
20-May-2011	HARPSpol	701.67331	04:03:32	4×600	874	679.461	0.461	-16.279	N
20-May-2011	HARPSpol	701.70345	04:46:56	4×600	597	679.470	0.470	-16.299	N

Table B2. Journal of NARVAL observations up to and including January 2015 of τ Boötis. Columns list the UT date, instrument used, the heliocentric Julian date (at midpoint of the series of 4 sub-exposures), the UT time (at midpoint of the series of 4 sub-exposures), the exposure time, the peak signal-to-noise ratio (SNR) of each observation (at around 700 nm for NARVAL), the rotational cycle from the ephemeris (from Equation 1), the rotational phase (0.0 being approximately the centre of the observing run), the radial velocity (RV) associated with each exposure, and whether a magnetic signature is detected (D; $fap < 10^{-5}$), marginally detected (M; $10^{-3} > fap > 10^{-5}$) or is below the detection threshold (N).

Date	Instrument	HJD (245 5000+)	UT (h:m:s)	T_{exp} (s)	SNR	Cycle	ϕ_{rot}	RV (km s^{-1})	Detection
23-Apr-2013	NARVAL	1405.57009	01:33:59	4×600	1493	891.961	-3.040	-16.727	N
24-Apr-2013	NARVAL	1406.53353	00:41:21	4×600	1365	892.251	-2.749	-16.124	D
24-Apr-2013	NARVAL	1407.41519	21:50:57	4×600	1521	892.518	-2.483	-16.631	N
04-May-2013	NARVAL	1417.46698	23:05:45	4×600	1491	895.552	0.552	-16.773	M
05-May-2013	NARVAL	1418.44661	22:36:27	4×600	1410	895.848	0.848	-16.938	D
11-May-2013	NARVAL	1424.42736	22:08:58	4×600	1507	897.653	2.653	-16.998	N
12-May-2013	NARVAL	1425.42272	22:02:19	4×600	1401	897.954	2.954	-16.669	D
13-May-2013	NARVAL	1426.44343	22:32:11	4×600	1521	898.262	3.262	-16.095	D
04-Dec-2013	NARVAL	1630.73709	05:46:20	4×600	1408	959.936	-3.064	-16.822	N
05-Dec-2013	NARVAL	1631.72401	05:27:25	4×600	1318	960.234	-2.766	-16.164	D
06-Dec-2013	NARVAL	1632.73127	05:37:48	4×600	1280	960.538	-2.462	-16.735	N
07-Dec-2013	NARVAL	1633.71947	05:20:42	4×600	1202	960.837	-2.164	-16.993	M
08-Dec-2013	NARVAL	1634.71910	05:20:05	4×600	1484	961.138	-1.862	-16.268	D
09-Dec-2013	NARVAL	1635.74031	05:50:32	4×600	1479	961.447	-1.553	-16.444	D
11-Dec-2013	NARVAL	1637.72461	05:27:44	4×600	1259	962.046	-0.954	-16.520	M
12-Dec-2013	NARVAL	1638.71993	05:20:54	4×600	1546	962.346	-0.654	-16.257	D
13-Dec-2013	NARVAL	1639.73536	05:43:02	4×600	1505	962.653	-0.347	-17.022	D
15-Dec-2013	NARVAL	1641.72308	05:25:09	4×600	1381	963.253	0.253	-16.116	N
17-Dec-2013	NARVAL	1643.75082	06:04:53	4×600	1483	963.865	0.865	-16.923	D
21-Dec-2013	NARVAL	1647.73550	05:42:25	4×600	1447	965.068	2.068	-16.403	N
04-May-2014	NARVAL	1782.47281	23:14:08	4×600	1304	1005.744	-2.256	-17.089	D
05-May-2014	NARVAL	1783.47546	23:17:58	4×600	1350	1006.046	-1.954	-16.397	N
07-May-2014	NARVAL	1785.46095	22:57:09	4×600	1079	1006.646	-1.354	-16.945	M
08-May-2014	NARVAL	1786.49026	23:39:24	4×600	1377	1006.957	-1.044	-16.668	M
09-May-2014	NARVAL	1787.48744	23:35:22	4×600	1374	1007.258	-0.742	-16.094	D
14-May-2014	NARVAL	1791.54389	00:56:51	4×600	1512	1008.482	0.482	-16.563	N
14-May-2014	NARVAL	1792.43744	22:23:36	4×600	954	1008.752	0.752	-17.089	N
15-May-2014	NARVAL	1793.48608	23:33:42	4×600	940	1009.069	1.069	-16.438	N
16-May-2014	NARVAL	1794.46699	23:06:15	4×600	892	1009.365	1.365	-16.345	N
17-May-2014	NARVAL	1795.47600	23:19:17	4×600	1312	1009.669	1.669	-17.048	M
18-May-2014	NARVAL	1796.45889	22:54:42	4×600	1295	1009.966	1.966	-16.671	M
06-Jan-2015	NARVAL	2028.73834	05:44:44	4×600	1511	1080.089	-1.911	-16.355	D
07-Jan-2015	NARVAL	2029.72424	05:24:19	4×520	1386	1080.387	-1.614	-16.372	D
08-Jan-2015	NARVAL	2030.74613	05:55:43	4×520	1401	1080.695	-1.305	-17.149	N
09-Jan-2015	NARVAL	2031.72258	05:21:41	4×600	1396	1080.990	-1.010	-16.673	D
10-Jan-2015	NARVAL	2032.73855	05:44:33	4×520	1442	1081.297	-0.704	-16.207	M
12-Jan-2015	NARVAL	2034.73935	05:45:29	4×520	1425	1081.901	-0.100	-16.988	D
18-Jan-2015	NARVAL	2040.67474	04:11:43	4×600	707	1083.692	1.692	-17.178	N

Table B3. Journal of NARVAL observations up to and including March through May 2015 of τ Boötis. Columns list the UT date, instrument used, the heliocentric Julian date (at midpoint of the series of 4 sub-exposures), the UT time (at midpoint of the series of 4 sub-exposures), the exposure time, the peak signal-to-noise ratio (SNR) of each observation (at around 700 nm for NARVAL), the rotational cycle from the ephemeris (from Equation 1), the radial velocity (RV) associated with each exposure, and whether a magnetic signature is detected (D; $fap < 10^{-5}$), marginally detected (M; $10^{-3} > fap > 10^{-5}$) or is below the detection threshold (N).

Date	Instrument	HJD (245 5000+)	UT (h:m:s)	T_{exp} (s)	SNR	Cycle	RV (km s^{-1})	Detection
12-Mar-2015	NARVAL	2093.60723	02:28:57	4×600	1300	1099.672	-17.103	N
13-Mar-2015	NARVAL	2094.57542	01:43:04	4×600	1387	1099.964	-16.769	M
17-Mar-2015	NARVAL	2098.60339	02:23:04	4×600	1243	1101.180	-16.307	D
02-Apr-2015	NARVAL	2114.54024	00:51:19	4×600	1567	1105.992	-16.685	M
13-Apr-2015	NARVAL	2126.44800	22:38:12	4×600	1357	1109.586	-17.002	M
14-Apr-2015	NARVAL	2127.37286	20:49:59	4×600	592	1109.866	-17.016	N
20-Apr-2015	NARVAL	2133.42700	22:07:56	4×600	1369	1111.693	-17.159	M
21-Apr-2015	NARVAL	2134.42323	22:02:30	4×600	590	1111.994	-16.650	N
23-Apr-2015	NARVAL	2136.45663	22:50:36	4×600	1446	1112.608	-17.010	D
30-Apr-2015	NARVAL	2142.52088	00:23:13	4×600	1385	1114.439	-16.554	N
11-May-2015	NARVAL	2154.47299	23:14:38	4×600	992	1118.047	-16.542	N
12-May-2015	NARVAL	2155.47975	23:24:25	4×600	1043	1118.351	-16.235	N
16-May-2015	NARVAL	2159.45312	22:46:16	4×600	1417	1119.550	-16.848	M
17-May-2015	NARVAL	2160.48669	23:34:39	4×600	1077	1119.862	-17.049	N
19-May-2015	NARVAL	2161.50449	00:00:21	4×700	472	1120.170	-16.243	N
27-May-2015	NARVAL	2170.37187	20:49:57	4×600	1527	1122.847	-17.025	D